## Politecnico di Torino

Ingegneria Elettronica (Electronic Engineering)
A.a. 2024/2025
Graduation Session December 2025

# Characterization and Modeling of a Si–PolySi Microring Resonator with Application in Neuromorphic Computing

Relatori:
Mariangela Gioannini
Marco Novarese

Candidato:
Simone Tamborrino

# Abstract

The objective of this thesis is to characterize and model an optical microring resonator (MRR) in the silicon-insulator-silicon capacitor platform (SISCAP) composed of an hybrid silicon–polysilicon (Si–PolySi) ring waveguides, here we investigate its potential for neuromorphic computing applications, specifically using the reservoir computing (RC) approach.

The first part of the work focuses on the study and analysis of the non-linear optical behavior of the Si–PolySi microring resonator: at high optical power injection, two-photon absorption (TPA) generates free carriers, which modify the refractive index through free-carrier dispersion (FCD). This leads to a power-dependent shift of the resonance wavelength and a distortion of the transmission spectrum, revealing the strong non-linear response of the ring. The dynamics of the free carriers create a temporal memory effect in the ring, which can be exploited as the nonlinear node of a reservoir computing network. In this configuration, the response of the system to a given input bit depends on the residual carrier population generated by the previous bits, enabling the processing of temporal correlations within the input sequence.

The experimental work includes a pump–probe setup, as it allows monitoring the carrier dynamics response of the device during operation in neuromorphic computing experiments.

As in previous studies on fully silicon microrings, the objective is to verify whether the carrier dynamics in the Si–PolySi ring can provide the non-linear and memory responses necessary for RC tasks. The specific application investigated in this thesis is the one-bit XOR predictor.

The main idea is to exploit the faster carrier dynamics in polysilicon, due to its shorter carrier lifetime compared to pure silicon, to achieve higher bitrates in temporal computing applications. However, laboratory measurements show that the prediction accuracy obtained from experimental traces is lower than that reported for full silicon rings in previous studies. At high bitrates, the ring response cannot follow the input accurately, as the trap-dominated dynamic of silicon prevails over the faster carrier response of polysilicon.

Furthermore, the thermal transient (often neglected in theory) is actually not negligible, and the output response is distorted due to thermal effects.

We therefore conclude that the two effects limit the performance of this device for reservoir computing applications.

This work provides a comprehensive characterization and modeling of Si–PolySi microrings, highlighting the limitations imposed by thermal effects and offering insights for future improvements in high-speed photonic neuromorphic computing.

# Summary

The use of silicon microring resonators in add-drop configuration has been widely explored as a nonlinear element within reservoir computing architectures. Silicon exhibits nonlinear mechanism such as Two-Photon Absorption (TPA) and Free-Carrier Dispersion (FCD) that can be advantageously exploited in neuromorphic and AI-oriented applications to enable high-speed and energy-efficient optical neural networks. In this thesis, the nonlinear node of the reservoir is implemented using a microring resonator based on the silicon–insulator–silicon capacitor (SISCAP) platform. The device consists of a hybrid silicon–polysilicon (Si–PolySi) ring waveguide, selected for its faster carrier dynamics due to the much shorter polysilicon carrier lifetime, on the order of a few hundred picoseconds, compared to crystalline silicon. The main objective is to evaluate whether this Si–PolySi microring can function as an effective nonlinear node for temporal reservoir computing and to compare its performance with pure-silicon microrings for the 1-bit delayed XOR task. The dominant mechanisms responsible for spectral distortion in microrings are Two-Photon-absorption (TPA) and Free-Carrier Absorption (FCA). These effects increase the optical loss and reduce the resonator quality factor. Free carriers also induce a refractive index change through FCD, which shifts the resonance towards shorter wavelengths. Conversely, carrier relaxation through Shockley-Read-Hall processes releases heat, increasing the ring temperature and causing a thermally induced red shift. The balance between these competing blue and red shift mechanisms defines the dynamic response of the resonator under high optical power.

Static measurements were first performed to characterize both Si and Si-PolySi rings. Linear transmission spectra were fitted to extract resonator parameters, while nonlinear steady-state measurements provided the resonance shift as a function of the input power. The Si-PolySi ring exhibits a significantly lower quality factor than a silicon ring, implying weaker nonlinear effects for the same circulating power. At high power injection, in steady-state condition, self-oscillation prevents stable acquisition of the nonlinear transmission spectrum, leading to deviations between measured and expected resonance shifts. Pump and probe measurements allow the monitoring and identification of nonlinear effects. Two optical signals, a high-power

pump and a low-power probe, are injected at adjacent resonances of the microring. The pump generates free carriers, while the probe monitors the corresponding resonance shift.

The pump-probe experiment was reproduced using isolated pulses and binary bit sequences at the input of the MRR. These measurements provide insight into how thermal and free-carrier effects evolve with bitrate. At low bitrates, logical “1” bits generate pronounced temperature peaks, inducing large thermally driven red shifts. Even though partial cooling occurs between bits, thermal dynamics remain dominant, strongly distorting the output waveform and making it highly sensitive to the chosen probe detuning. As the bitrate increases, temperature excursions become smaller, but the reduced cooling time leads to a quasi-steady thermal offset.

Above approximately 500 Mbps, the bit period becomes too short for full carrier recombination in silicon, causing carrier accumulation. This results in a sustained FCD-induced blue shift superimposed on the thermal drift. The combined shift depends strongly on bitrate, rendering detuning of the probe signal with respect to the cold resonance ineffective. At very high bitrates, the contribution of shorter carrier lifetime of polysilicon is negligible, with silicon carriers dominating the refractive-index dynamics. Meanwhile, the overall resonance shift decreases in magnitude, reducing probe-signal visibility and limiting experimental measurability.

The performance of the Si-PolySi microring as a nonlinear node for the 1-bit delayed XOR task reflects these limitations. With a fixed detuning, the experimental accuracy varies significantly with bitrate. At 50 Mbps and 10 dBm pump power, an accuracy of about 92% is achieved, confirming the feasibility of the experiment despite thermal distortion, but still below the ideal 100% obtained with pure-silicon microrings. The faster carrier dynamics of polysilicon do not provide an improvement: in simulation, accuracy decreases from 93% at 1 GHz to 82% at 5 GHz and 68% at 10 GHz. At such high speeds, the combined detuning sensitivity, measurement noise, and setup limitations make experimental validation impractical.

Simulations using the theoretical model yield higher accuracies, particularly in the intermediate bitrate range (100-500 Mbps), where thermal drift is more stable. Increasing the number of virtual nodes slightly improves performance: raising $N_v$ from 3 to 6 suffices to reach 100% accuracy in simulations, with a slight improvement also observed experimentally. Simulations also show that lowering pump power reduces both FCD and thermally induced resonance shifts, enabling 100% simulated accuracy even with $N_v = 3$. Experimentally, however, reducing pump power decreases FCD induced resonance shifts making the probe trace more subjected to noise, with a consequent degradation in accuracy. Experimentally, at both 6 dBm and 10 dBm pump power, the classification accuracy obtained from the probe is consistently lower than that extracted directly from the pump input signal, confirming that, under the explored operating conditions, the hybrid Si–PolySi resonator does not offer any computational advantage.

# Table of Contents

# List of Tables

# List of Figures

# Chapter 1

# Introduction

Neuromorphic computing is a computing techinique that aim to emulate the behavior of biological neurons and their communication mechanisms using electronic circuits. In recent years, technological progress has accelerated rapidly, driven by increasingly powerful digital processing units and more sophisticated algorithms. Among these, artificial neural networks (ANNs) have emerged as one of the most influential tools in modern machine learning and artificial intelligence.

Among neuromorphic architectures, Reservoir Computing (RC) has attracted growing interests due to its trade-off between performance and training complexity [1]. RC is inspired by recurrent neural networks (RNNs): the input signal excites the nonlinear dynamics of a high dimensional network, typically composed of many nodes, with fixed and sparsely connected weights. The network transforms the input into a higher-dimensional representation, enhancing the linear separability of the data. In contrast to conventional neural networks, in RC only the readout layer is trained, as the reservoir's complex nonlinear dynamics inherently provide the required computational richness. In this work will be analyzed the computational task of the 1-Bit Delayed XOR, since the XOR operation is a clear example of an operation that cannot be linearly separated in a two-dimensional space, but it becomes linearly separable in a three-dimensional space, making the classification problem simple and linear.

The integration of silicon photonics has opened a new path toward implementing neural network based computation beyond traditional electronic platforms. Photonics infact offers several key advantages, including large bandwidth, intrinsic parallelism enabled by wavelength-division multiplexing (WDM), improved energy efficiency, low latency, high throughput, and immunity to electromagnetic interference. Within this context, optical microring resonators (MRRs) stand out as promising building blocks for neuromorphic systems thanks to their nonlinear behavior.

In other works [2, 3, 4] the use of a silicon microring resonator in add-drop configuration as a nonlinear element within a reservoir computing neural architecture has been discussed. Silicon as an optical medium exhibits nonlinear absorption mechanisms that introduce power dependent losses. These effects are particularly pronounced in microring resonators, where the circulating optical intensity can be significantly enhanced, altering the spectral response. However, these nonlinearities that create challenges in classical photonics can be advantageously exploited for neuromorphic and AI-related tasks, enabling optical neural networks capable of operating with high speed and low energy consumption.

In this thesis, the nonlinear node of the reservoir is not a pure silicon microring but a microring based on the silicon–insulator–silicon capacitor (SISCAP) platform. The device consists of a hybrid silicon–polysilicon (Si–PolySi) ring waveguide, chosen specifically for its faster carrier dynamics enabled by the reduced carrier lifetime of polysilicon compared to pure crystalline silicon. The aim of this work is therefore to assess whether the Si–PolySi microring can serve as an effective nonlinear node for temporal reservoir computing and to compare its performance with pure silicon solutions for the 1-Bit Delayed XOR computational task.

This thesis is structured as follows. First, the fundamental principles of microring resonators (MRRs) are introduced, together with the key parameters that describe their behavior, with particular attention to the modeling of nonlinear effects. The characterization of the specific ring used in this work is then presented. Subsequently, the model developed by Marco Novarese in [5] is adapted to the characteristics of the hybrid Si-PolySi ring under study. The model is experimentally validated, and finally, the neural network developed by Salvatore Salpietro in [3] is applied in order to evaluate the performance of the device and compare it with that of a pure silicon ring.

## 1.1 Introduction to Artificial Neural Networks

Artificial neural networks (ANNs) are computational models inspired by the human brain, designed to emulate how neurons communicate and process information. They consist of interconnected nodes, or artificial neurons, which sum their weighted inputs and apply a nonlinear activation function:

$$y = f_a\left(\sum_{i=1}^{N_u} w_i u_i + w_0\right),$$

where $u_i$ are the inputs, $w_i$ the weights, $w_0$ the bias, $N_u$ the number of inputs, and $f_a$ a nonlinear function. The weights determine the influence of each input and are adjusted during training to guide the network toward the desired output.

Nonlinear activation functions are essential, as they allow the network to model complex relationships; without them, multiple layers collapse to the equivalent of a single neuron, limiting computational power. This capability is crucial for solving problems that are not linearly separable, such as the 1-bit delayed XOR task. By stacking multiple layers with nonlinear activations, the network transforms inputs into a higher-dimensional space, increasing the likelihood that the final layer can linearly separate the outputs.

Training a neural network typically involves two stages: **feedforward propagation**, where inputs pass through the layers to produce outputs, and **backpropagation**, where errors are propagated backward to update the weights. Details of the training procedure are discussed in subsequent sections.

### 1.1.1 Structure and functioning of Artificial Neural Networks

Neural networks can be classified into two main categories: **feedforward neural networks (FFNNs)** and **recurrent neural networks (RNNs)**. Both types are typically organized into an *input layer*, one or more *hidden layers*, and an *output layer*. The key components of these networks are:

- **Input vector:**

$$\mathbf{u}(n) = \begin{pmatrix} u_1(n) \\ u_2(n) \\ \vdots \\ u_{N_u}(n) \end{pmatrix} \in \mathbb{R}^{N_u},$$

  where $N_u$ is the input dimensionality and $n$ denotes the time step.

- **Network state vector:**

$$\mathbf{x}(n) = \begin{pmatrix} x_1(n) \\ x_2(n) \\ \vdots \\ x_{N_x}(n) \end{pmatrix} \in \mathbb{R}^{N_x},$$

  which represents the internal states responsible for memory and information processing.

- **Output vector:**

$$\mathbf{y}(n) = \begin{pmatrix} y_1(n) \\ y_2(n) \\ \vdots \\ y_{N_y}(n) \end{pmatrix} \in \mathbb{R}^{N_y},$$

where $N_y$ is the output dimensionality.

- **Weight matrices:**
  - Input-to-hidden weights: $\mathbf{W}_u = (w_{u,ij}) \in \mathbb{R}^{N_x \times N_u}$
  - Hidden-to-hidden weights: $\mathbf{W}_x = (w_{x,ij}) \in \mathbb{R}^{N_x \times N_x}$
  - Hidden-to-output weights: $\mathbf{W}_y = (w_{y,ij}) \in \mathbb{R}^{N_y \times N_x}$
  - Optional output-to-hidden feedback: $\mathbf{W}_{fb} = (w_{fb,ij}) \in \mathbb{R}^{N_x \times N_y}$, which enhances the network's memory.

### General Training Procedure for Artificial Neural Networks

Neural networks can be trained using three main learning paradigms:

1. **Supervised learning:** The network is trained on a dataset consisting of inputs and their corresponding target outputs. The goal is to minimize the error between the predicted and desired outputs.
2. **Unsupervised learning:** No target outputs are provided. The network identifies patterns or structures within the data.
3. **Reinforcement learning:** The network learns through trial and error to achieve a predefined goal, receiving feedback in the form of rewards or penalties.

In supervised learning, a common training method is *gradient descent*, which iteratively updates the network weights to minimize a loss function $L$. The weight update at step $i$ is given by:

$$\mathbf{w}' = \mathbf{w}_i - \eta \frac{\partial L}{\partial \mathbf{w}_i},$$

where $\mathbf{w}'$ are the updated weights, $\eta$ is the learning rate controlling the convergence speed, and $L$ is the loss function.

To improve convergence, input features can be scaled using:

- **Min-max scaling:** Normalizes features within a specific range, e.g., [0,1] or [-1,1].
- **Z-score normalization:** Centers features around zero:

$$u_i = \frac{u_i - \mu_i}{\sigma_i},$$

where $\mu_i$ and $\sigma_i$ are the mean and standard deviation of the feature $u_i$.

Training recurrent neural networks (RNNs) is more complex due to temporal dependencies. The *backpropagation through time (BPTT)* algorithm unrolls the network over time, updating all weights, which requires significant computational resources.

An alternative approach is *reservoir computing*, which simplifies training by keeping the internal weights of the reservoir fixed and training only the readout layer connecting reservoir states to outputs, enabling faster and more efficient learning.

### Feedforward Neural Networks

Feedforward neural networks (FFNNs) are composed of sequential layers: an input layer, one or more hidden layers, and an output layer (see Figure 1.1). In these networks, each neuron is connected only to neurons in the previous layer through weighted connections, and information flows in one direction, from input to output.

FFNNs have no memory of past activations; their output depends solely on the current input. The state of a neuron in layer $i + 1$ is given by:

$$\mathbf{x}_{i+1} = f(\mathbf{W}_x \mathbf{x}_i + \mathbf{b}_i),$$

where $f$ is a nonlinear activation function, $\mathbf{W}_x$ is the weight matrix connecting layer $i$ to $i + 1$, and $\mathbf{b}_i$ is the bias vector. If a neuron's input is inactive, its output remains inactive.

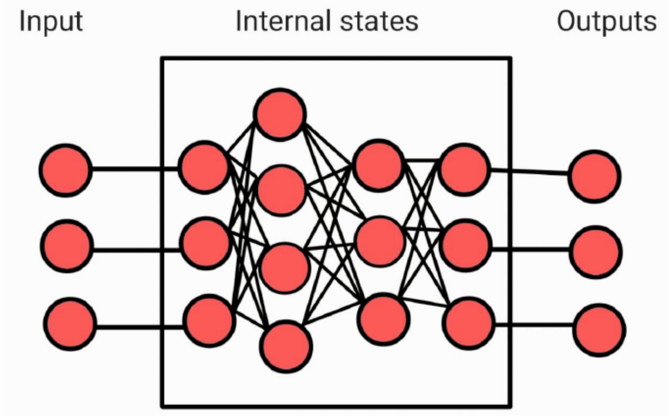

**Figure 1.1:** General scheme of a feedforward neural network. Red circles represent artificial neurons. Reprinted from [3].

### Recurrent Neural Networks

Recurrent neural networks (RNNs) differ from FFNNs because they have memory. Feedback loops can exist within the same neuron or directed to previous layers (see Figure 1.2). All connections must be trained. Consequently, the internal states of RNNs depend on both the current input and past states, providing the network with memory. This makes RNNs suitable for tasks like time series prediction or natural language processing.

The state update equation for RNNs is:

$$\mathbf{x}(n+1) = f(\mathbf{W}_u\mathbf{u}(n+1) + \mathbf{W}_x\mathbf{x}(n) + \mathbf{W}_{fb}\mathbf{y}(n)),$$

where $\mathbf{W}_u$, $\mathbf{W}_x$, and $\mathbf{W}_{fb}$ are the input, hidden, and feedback weight matrices, respectively, and $f$ is a nonlinear activation function such as tanh or the logistic sigmoid. The output is calculated as:

$$\hat{\mathbf{y}}(n+1) = g(\mathbf{W}_y\mathbf{x}(n+1) + \mathbf{W}_y\mathbf{u}(n+1)),$$

with $g$ as the output activation function.

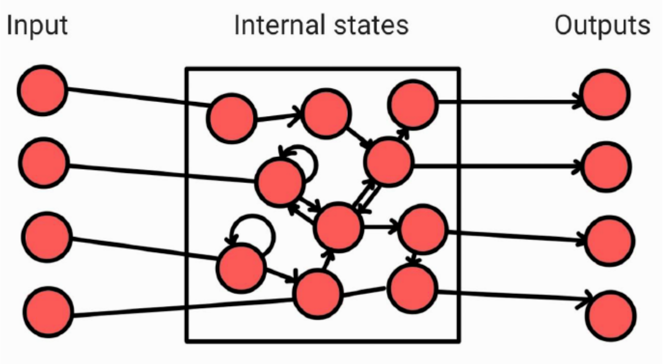

**Figure 1.2:** General scheme of a recurrent neural network. Reprinted from [3].

### Reservoir Computing

Reservoir computing (RC) is a technique based on RNNs, specifically for this thesis work the Echo State Network (ESN) will be employed. In RC, the internal weights of the reservoir are fixed and randomly assigned, while only the connections from the readout layer to the output layer are trained (see Figure 1.3). The reservoir transforms inputs through nonlinear dynamics into a higher-dimensional space, enhancing the linear separability of the data. For example, the result of the XOR operation cannot be linearly separated in a two-dimensional space, but by mapping it into a three-dimensional space, the classification problem becomes simple and linear.

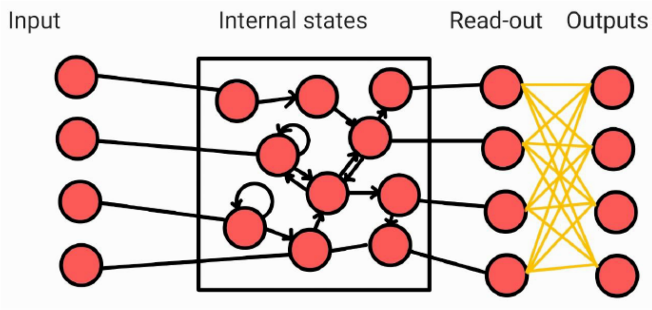

**Figure 1.3:** General scheme of a reservoir computing system. Yellow connections represent trainable weights. Reprinted from [3].

Reservoir computing can be implemented in two main ways: spatial reservoirs, where neurons are distributed and connected in space, and delay-based reservoirs (temporal multiplexing), where inputs are sequentially injected into a single nonlinear node. In this work, we employ temporal multiplexing, a technique commonly used in delay-based photonic reservoirs using the MRR as the nonlinear node. Temporal multiplexing increases the effective dimensionality of the reservoir by creating virtual nodes along a feedback delay line. These virtual nodes represent delayed versions of the nonlinearly transformed signal, separated by a temporal interval $\theta$. The delay line, whose length and material determine the memory and dynamics of the system, allows the reservoir to retain past information and improves performance on tasks requiring extended temporal memory.

The main steps of reservoir computing are:

1. **Reservoir preparation:** Split the dataset into training and test sets (e.g., 70%-30%). Input signals $\mathbf{u}_{\text{train}}(t)$ generate internal states $\mathbf{x}_i(t)$ in the readout layer.

2. **Execution:** Collect readout states $\mathbf{x}_{\text{train},i}(t)$ and compute the output as a weighted combination. Only the readout weights are trained.

3. **Role of the readout function $G$:** The function $G$ maps readout states to the desired output. Training adjusts $G$ to minimize the difference between predicted $\hat{\mathbf{y}}(t)$ and target $\mathbf{y}(t)$.

4. **Training:** Minimize the loss function $L(\mathbf{y}_{\text{train}}, \hat{\mathbf{y}})$ over all training samples.

5. **Testing:** Evaluate the reservoir on the test set, typically using accuracy as the performance metric.

### Linear Regression

Linear Regression is a supervised learning technique used to estimate a linear relationship between two variables. In the context of this thesis, it is employed to map the states of the readout layer to the desired outputs by finding the optimal weight matrix $\mathbf{W}_y$ that minimizes the Mean Squared Error (MSE) between the predicted output $\hat{\mathbf{y}}(t)$ and the target output $\mathbf{y}_{\text{train}}(t)$:

$$\mathbf{W}_y = \arg\min_{\mathbf{W}_y} \sum_{i=1}^{N_x} \left(\mathbf{W}_y \mathbf{x}_i - y_{i,\text{train}}\right)^2, \tag{1.1}$$

which is equivalent to the closed-form solution:

$$\mathbf{W}_y = (\mathbf{X}^{\mathrm{T}}\mathbf{X})^{-1}\mathbf{X}^{\mathrm{T}}\mathbf{Y}_{\text{train}}, \tag{1.2}$$

where:

- $\mathbf{X}$ is the matrix of reservoir states (each row corresponds to a state at time $t$),
- $\mathbf{X}^{\mathrm{T}}$ is the transpose of $\mathbf{X}$,
- $\mathbf{Y}_{\text{train}}$ is the vector of target outputs,
- $(\mathbf{X}^{\mathrm{T}}\mathbf{X})^{-1}$ is the Moore-Penrose pseudo-inverse of the product.

Squaring the differences gives more weight to larger errors. Once $\mathbf{W}_y$ is trained on the dataset, the readout function $G$ can predict outputs for unseen inputs, with accuracy depending on the amount of training data.

Linear regression can also be implemented in hardware [**ref6**]. For classification tasks, a typical output encoding is *one-hot encoding*, where the output vector has a position representing the class and a value representing the probability of belonging to that class. The *winner-takes-all* technique, which selects the class with the highest value, is used in this thesis.

### Ridge Regression

Linear regression can suffer from two main problems: *overfitting* and *underfitting*. Overfitting occurs when the model is too complex and fits the training data too well, capturing noise and random fluctuations, which reduces its generalization capability. Underfitting happens when the model is too simple, failing to capture the underlying patterns of the data. Figure **??** illustrates an example of overfitting in (a) and a correct model fit in (b).

One solution to overfitting is to reduce the number of features or to use *ridge regression*, which introduces regularization by adding a penalty term $\lambda$ to the loss function. Unlike simple linear regression, ridge regression reduces the magnitude of the weights without removing features. A smaller weight magnitude corresponds to a less complex model.

Common regularization methods include:

- **LASSO (L1 penalty)**: penalizes the sum of absolute values of the weights. The loss function is

$$\text{Cost Function} = \sum(\text{squared residuals}) + \lambda \sum |w_i|.$$

- **Ridge Regression (L2 penalty)**: penalizes the sum of squares of the weights. The loss function is

$$\text{Cost Function} = \sum(\text{squared residuals}) + \lambda \sum |w_i|^2.$$

Ridge regression is particularly effective when variables are highly correlated. It minimizes the following objective:

$$\mathbf{W}_y = \arg\min_{\mathbf{W}_y} \sum_{i=1}^{N_x} (\mathbf{W}_y \mathbf{x}_i - y_{i,\text{train}})^2 + \lambda \|\mathbf{W}_y\|_2^2, \tag{1.3}$$

where $\|\mathbf{W}_y\|_2^2$ is the squared norm of the weight matrix, preventing the weights from growing too large.

To solve for $\mathbf{W}_y$, we compute the gradient with respect to $\mathbf{W}_y$ and set it to zero:

$$\frac{\partial}{\partial \mathbf{W}_y} \Big( \|\mathbf{Y}_{\text{train}} - \mathbf{W}_y \mathbf{X}\|_2^2 + \lambda \|\mathbf{W}_y\|_2^2 \Big) = 0.$$

Expanding and simplifying gives:

$$-2\mathbf{Y}_{\text{train}} \mathbf{X}^{\mathrm{T}} + 2\mathbf{W}_y \mathbf{X}\mathbf{X}^{\mathrm{T}} + 2\lambda \mathbf{W}_y = 0,$$

which leads to the closed-form solution:

$$\mathbf{W}_y = (\mathbf{Y}_{\text{train}} \mathbf{X}^{\mathrm{T}})(\mathbf{X}\mathbf{X}^{\mathrm{T}} + \lambda \mathbf{I})^{-1}, \tag{1.4}$$

where $\mathbf{I}$ is the identity matrix. A larger $\lambda$ penalizes large weights more, reducing the model's sensitivity to individual training examples and improving generalization.

### Cross Validation

The choice of $\lambda$ is crucial: small values may lead to overfitting, while large values may underfit the model. *Cross-validation* is a standard technique to select the optimal $\lambda$. Among the common methods are 5-Fold or 10-Fold Cross-Validation.

In $k$-fold cross-validation, the dataset is split into $k$ subsets, called folds. For a chosen $\lambda$, the model is trained on $k-1$ folds and tested on the remaining fold, calculating the accuracy. This process is repeated $k$ times, each time using a different fold as the test set. The average accuracy over the $k$ iterations is then computed.

The procedure is repeated for different $\lambda$ values. The optimal $\lambda$ is the one that maximizes the average accuracy, balancing model complexity and generalization.

# Chapter 2

# Modelling of microring resonators

## 2.1 Fundamental concepts of microring resonators

Microring resonators play a crucial role in the advancement of silicon photonics, thanks to significant advances in photonic integration and the availability of CMOS-compatible fabrication technologies.

A generic ring resonator consists of an optical waveguide that is looped back on itself and a coupling mechanism to access the loop. The resonance occurs when the optical path length of the loop is an integer multiple of the wavelength of the optical waves at the input.

In this condition, the waves circulating in the loop accumulate a round-trip phase shift equal to an integer multiple of $2\pi$, so they interfere constructively, and the cavity is in resonance [6].

As a result, ring resonators support multiple resonant modes, whose spacing, the free spectral range (FSR), depends on the optical length of the resonator, and therefore on its radius.

The microring resonator can be implemented in two different configurations: the *all-pass* and the *add-drop*. The first one consists of a single bus waveguide placed adjacent to a closed-loop waveguide, while the second one, which is the configuration analyzed in this work, includes two bus waveguides coupled to the ring. Figure 2.1 illustrates the schematic of the MRR in both the configurations.

Light can be coupled into the MRR through evanescent coupling from one waveguide in the *all-pass* configuration, or from two straight waveguides in the *add-drop* configuration, represented by the coupling coefficient $\kappa$.

In the add-drop configuration, destructive interference takes place at the through port, resulting in a minimum of transmitted power, while the drop port exhibits a

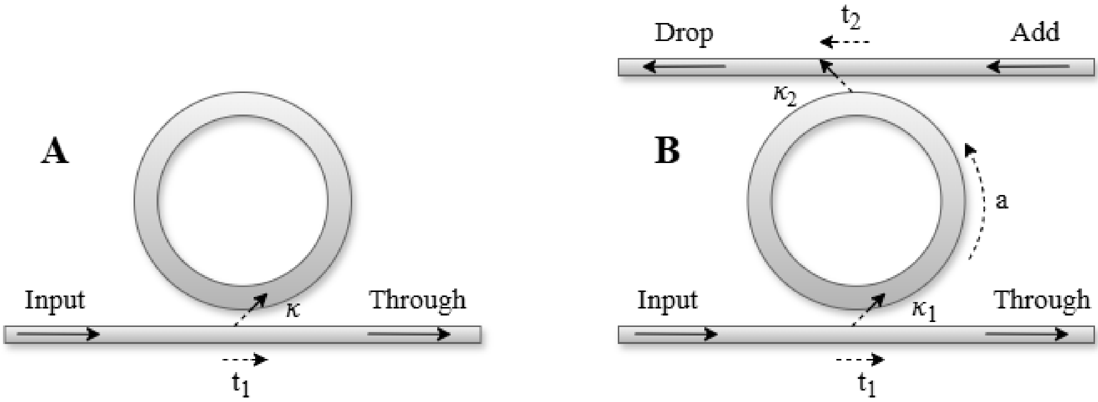

**Figure 2.1:** (A) All-pass and (B) add-drop ring resonator configurations.

maximum in output power due to the circulating power enhancement. Therefore, a MRR supports multiple resonances, meaning that its spectral response shows periodic peaks and dips at the drop and through ports, respectively, as illustrated in Fig. 2.2.

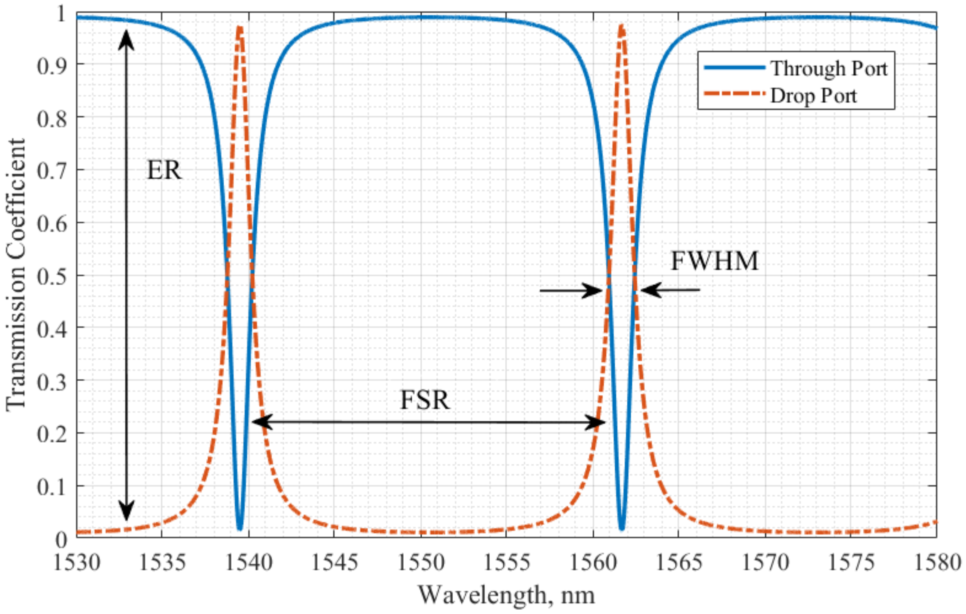

**Figure 2.2:** Spectral response of an add-drop MRR. The extinction ratio (ER) is defined as: $\mathrm{ER} = \frac{P_{\mathrm{thr,out,res}}}{P_{\mathrm{thr,res}}}$, where $P_{\mathrm{thr,out,res}}$ and $P_{\mathrm{thr,res}}$ are the output powers at the through port out of resonance and at resonance, respectively.

The resonance wavelength $\lambda_0$ for a microring is given by:

$$\lambda_0 = \frac{n_{\text{eff},0}\,L}{m}, \qquad m = 1, 2, 3, \ldots \tag{2.1}$$

where $n_{\text{eff},0}$ is the effective refractive index of the waveguide, $L$ is the total length of the MRR, and $m$ is an integer representing the resonance order.

The coupling loss in the bus-ring coupling region is indicated by the parameter $\eta^2$. Defining $P_{\text{bus}}$ as the power entering the coupler, the power loss per round trip in this region can be expressed as $\eta^2 \cdot P_{\text{bus}}$.

Here we assume that the coupling coefficients of the top and bottom bus waveguides, i.e., $\kappa_1$ and $\kappa_2$ respectively, are equal. This assumption is not true in the case of Si-PolySi ring analyzed in this work, where they are generally different.

The power conservation in the bus-ring coupling region is therefore given by:

$$t^2 + \kappa^2(1 - \eta^2) + \eta^2 = 1, \tag{2.2}$$

from which we obtain:

$$t^2 = (1 - \kappa^2)(1 - \eta^2). \tag{2.3}$$

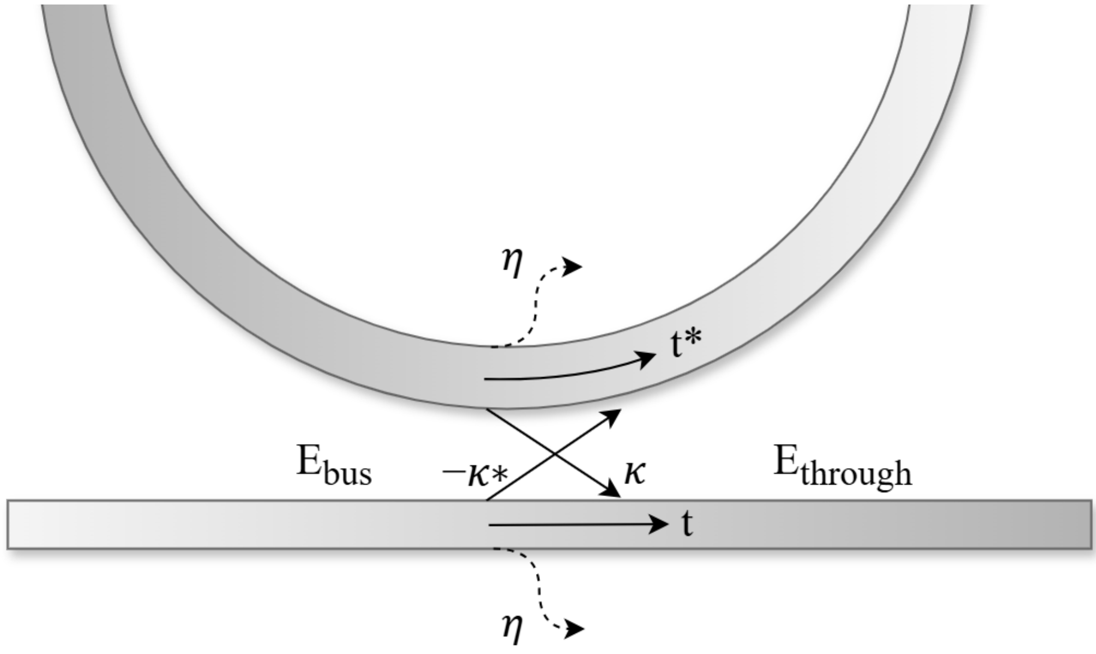

**Figure 2.3:** Zoom in the bus-ring coupling region.

From Fig. 2.3 we can observe a zoom in the bus-ring coupling region. The parameter $t$ represents the proportion of field that remains in the bus waveguide after passing through the coupler, while $\kappa$ describes the fraction of field traveling along the bus waveguide that is actually coupled into the microring.

During propagation in the ring, the optical field experiences modal losses, which can be expressed as:

$$a = e^{-\alpha_{\text{eff}} L/2}, \tag{2.4}$$

where the effective loss coefficient $\alpha_{\text{eff}}$ is defined as:

$$\alpha_{\text{eff}} = \alpha_0 + \alpha_{\text{rad}}, \tag{2.5}$$

with $\alpha_0$ representing the linear losses due to light scattering, residual doping, and single-photon absorption, and $\alpha_{\text{rad}}$ representing the losses due to light irradiated into the cladding.

With this formulation, the power transmission coefficients at the through port is given by:

$$T_{\text{thr}} = t^2 \frac{\left|1-(1-\eta^2)ae^{j\theta}\right|^2}{\left|1-t^2ae^{j\theta}\right|^2}, \tag{2.6}$$

while at the drop port it is as follows:

$$T_{\text{drop}} = \frac{\kappa^4(1-\eta^2)^2 a}{\left|1-t^2ae^{j\theta}\right|^2}. \tag{2.7}$$

To obtain the circulating power inside the ring, we consider that the total circulating field is the sum of all contributions associated with the multiple round trips within the ring. The first term corresponds to the input field $E_{\text{in}}$ in the add-drop MRR, given by $-\kappa \cdot (1-\eta^2)E_{\text{in}}$.

All subsequent terms can be expressed as:

$$E_c(\omega) = -\kappa \cdot (1-\eta^2)E_{\text{in}}(1 + t^2ae^{j\theta} + t^4a^2e^{2j\theta} + \dots), \tag{2.8}$$

where the series

$$1 + t^2ae^{j\theta} + t^4a^2e^{2j\theta} + \dots$$

is a geometric progression that can be written as:

$$\frac{1}{1-t^2ae^{j\theta}} = \sum_{n=0}^{\infty}(t^2ae^{j\theta})^n.$$

Therefore, the total circulating field becomes:

$$E_c(\omega) = -\frac{\kappa(1-\eta^2)E_{\text{in}}}{1-t^2ae^{j\theta}},$$

and the corresponding circulating power is:

$$P_c = |E_c|^2 = P_{\text{bus}} \cdot \frac{\kappa^2(1-\eta^2)}{|1 - t^2 a e^{j\theta}|^2}. \tag{2.9}$$

Here, $\theta$ is the total phase variation per round trip, expressed as:

$$\theta = \theta_0 + \frac{n_g}{c}(\omega - \omega_0)L, \tag{2.10}$$

where $\theta_0$ is the phase variation per round trip at the reference angular frequency $\omega_0$, and $n_g$ is the group refractive index of the resonator mode, which depends on the effective refractive index:

$$n_g = n_{\text{eff},0} - \lambda \frac{\partial n_{\text{eff},0}}{\partial \lambda}. \tag{2.11}$$

This definition accounts for the dispersion of the effective refractive index of the propagating mode in the waveguide.

Other important figures of merit (FOMs) in the description of microring resonators are the free spectral range (FSR), quality factor ($Q$), and finesse ($\mathcal{F}$). The FSR corresponds to the wavelength spacing between two adjacent resonance peaks, whereas the quality factor characterizes the sharpness of a specific resonance. It is defined as:

$$Q = \frac{\lambda_0}{\text{FWHM}}, \tag{2.12}$$

where FWHM is the full-width at half-maximum of the resonance peak, as illustrated in Figure 2.2.

The quality factor also provides an indication of the circulating power $P_c$ in the MRR: a larger $Q$ results in a higher $P_c$, which leads to stronger non-linear effects compared to a resonator with smaller $Q$, given the same input power and round-trip losses.

The finesse ($\mathcal{F}$) is defined as:

$$\mathcal{F} = \frac{\text{FSR}}{\text{FWHM}}, \tag{2.13}$$

where the *Free Spectral Range* (FSR) represents the wavelength spacing between two consecutive resonances, and the *Full Width at Half Maximum* (FWHM) denotes the width of a resonance at half of its maximum intensity.

For an add-drop ring resonator with $t_1 = t_2 = t$, the finesse can be expressed as:

$$\mathcal{F} = \frac{\pi t \sqrt{a}}{1 - t^2 a}. \tag{2.14}$$

Assuming the case where $\kappa \ll 1$ and both propagation and coupling losses are negligible ($a = 1$, $\eta = 0$), it can be demonstrated that:

$$t^2 = (1-\kappa^2)(1-\eta^2) \approx 1.$$

The resulting finesse $\mathcal{F}$ is therefore given by:

$$\mathcal{F} = \frac{\pi\sqrt{t^2 a}}{1-t^2 a} = \frac{\pi t}{1-t^2} \approx \frac{\pi}{\kappa^2}.$$

From this, it follows that:

$$\kappa^2 \approx \frac{\pi}{\mathcal{F}}.$$

Hence, the circulating power at resonance is:

$$P_c = P_{\text{bus}} \cdot \frac{\pi}{F} \cdot \frac{1}{(1-t^2)^2} = P_{\text{bus}} \cdot \frac{\mathcal{F}}{\pi t^2} \approx P_{\text{bus}} \cdot \frac{\mathcal{F}}{\pi}.$$

Thus, the ratio between the circulating power and the input power is:

$$\frac{P_c}{P_{\text{bus}}} = \frac{\mathcal{F}}{\pi}.$$

In the general case, considering non-negligible propagation and coupling losses, the circulating power $P_c$ at resonance can be expressed in terms of the self-coupling coefficient $t$ and the coupling coefficient $k$ as:

$$P_c = k^2\, P_{\text{bus}}\, \frac{(1-\eta^2)^2}{|1-t^2 a|^2}. \tag{2.15}$$

By solving for $t$ in terms of the finesse $F$ and the round-trip losses $a$, the expression can be simplified to a compact form:

$$P_c = P_{\text{bus}}(1-\eta^2)\frac{\mathcal{F}^2}{\pi^2}\left[\frac{4\mathcal{F}^2(1-\eta^2)}{2\pi^2 + 4F^2 - 2\pi\sqrt{\pi^2 + 4\mathcal{F}^2}} - \frac{1}{a}\right]. \tag{2.16}$$

Finally, expressing the finesse in terms of the quality factor $Q$ via

$$\mathcal{F} = \frac{Q\,\lambda_{\text{res}}}{n_g L},$$

we obtain a final formula for the circulating power in terms of $Q$:

$$P_c = P_{\text{bus}}\,(1-\eta^2)\,\frac{\left(\frac{Q\,\lambda_{\text{res}}}{n_g L}\right)^2}{\pi^2}\left[\frac{4\left(\frac{Q\,\lambda_{\text{res}}}{n_g L}\right)^2(1-\eta^2)}{2\pi^2 + 4\left(\frac{Q\,\lambda_{\text{res}}}{n_g L}\right)^2 - 2\pi\sqrt{\pi^2 + 4\left(\frac{Q\,\lambda_{\text{res}}}{n_g L}\right)^2}} - \frac{1}{a}\right]. \tag{2.17}$$

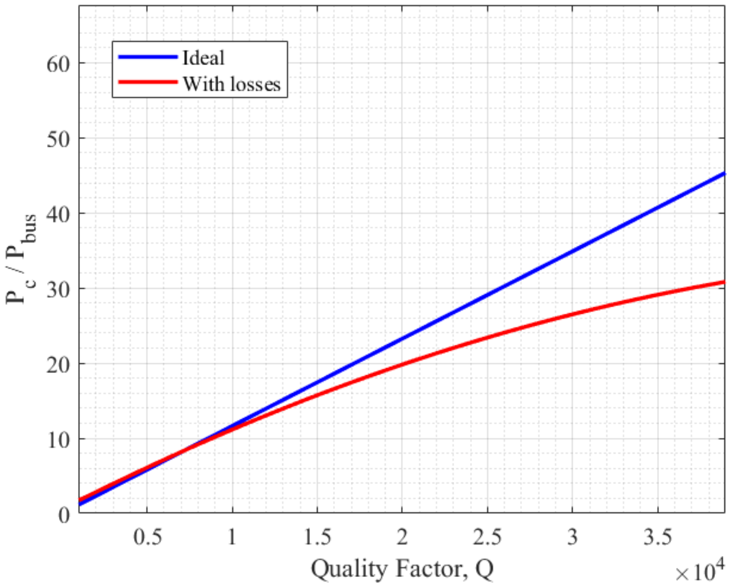

**Figure 2.4:** Comparison of the ratio between $P_c$ and $P_{bus}$ as a function of the finesse at resonance, with and without losses. The blue line represents the ideal case without losses, while the red line corresponds to the case including losses with $a = 0.9928$, $\eta_2 = 0.0073$, and $L = 79.42\ \mu$m.

This expression provides a direct relationship between the circulating power in the microring and the quality factor $Q$, taking into account both coupling and propagation losses.

In this work, the microring resonator adopts the configuration shown in Fig. 2.5, where the two through ports (Port 1 and Port 2) share the same input. The light enters from a single input port and encounters a splitter that divides it into the two bus waveguides.

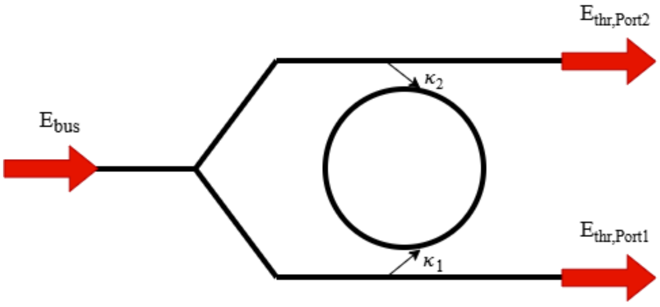

**Figure 2.5:** Ring configuration with a single input and a splitter.

In this configuration, the output power can be collected either from the top or bottom right output ports, which are both considered through ports. For convenience, these ports are labeled as Port 1 and Port 2. Accordingly, eq. 2.6 can be expressed for each port as follows.

At Port 1, the transmission is given by:

$$T_{\text{thr, Port1}} = \left| \frac{t_2 - \kappa_1^2 t_2 a e^{j\theta}(1-\eta^2)}{1 - t_1 t_2 a e^{j\theta}} \right|^2, \tag{2.18}$$

while at Port 2, it becomes:

$$T_{\text{thr, Port2}} = \left| \frac{t_2 - \kappa_2^2 t_1 a e^{j\theta}(1-\eta^2)}{1 - t_1 t_2 a e^{j\theta}} \right|^2. \tag{2.19}$$

Figure 2.6 shows an example of the transmission spectra at both port 1 and port 2 for a microring resonator with a radius of $r = 5\ \mu$m.

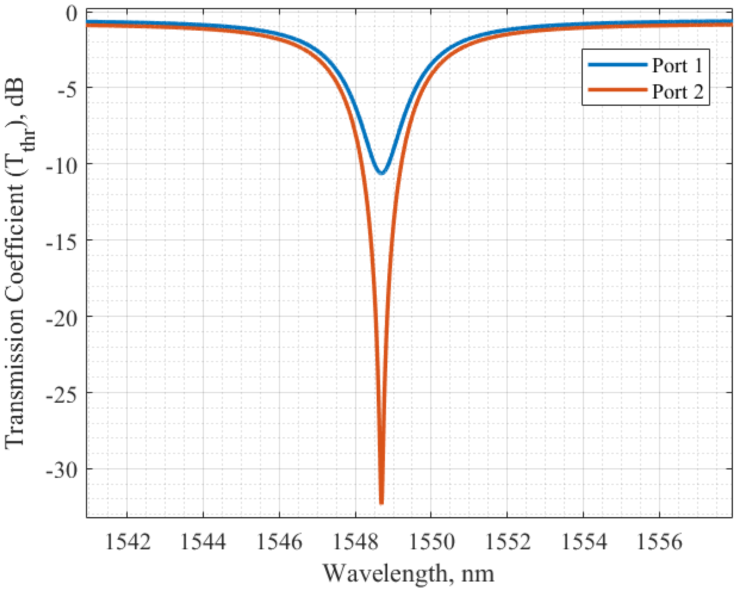

**Figure 2.6:** Spectral response of a ring resonator with radius $r = 2\mu m$ at Port 1 and Port 2 with the parameters: $\kappa_1 = 0.17$, $\kappa_2 = 0.21$, $\alpha_0 = 1.02$dB/cm, $\alpha_{rad} = 1.73$dB/cm, $n_g = 4.2$, $n_{eff} = 2.35$, $\eta^2 = 0.004$.

## 2.2 Thermal model

It is crucial to analyze the thermal behavior of the MRR to understand the influence of temperature on the silicon and polysilicon refractive index. Relaxation and recombination of free carriers, generated by TPA and FCA, result in self-heating of the MRR, which can be modeled by its thermal impedance $Z_T$, which for strip waveguides, that is the case analyzed in this work, is defined as:

$$Z_T = \frac{\Delta T}{P_{\text{abs}}} \tag{2.20}$$

with $\Delta T = T_{\max} - T_0$. Here, $T_{\max}$ represents the internal core temperature reached as a consequence of the absorbed power $P_{\text{abs}}$, starting from the ambient temperature $T_0$, set at $293.15K$.

A larger value of $Z_T$ corresponds to a poorer thermal conductivity, meaning that heat remains confined within the MRR due to inefficient transfer towards the substrate.

Thermal impedance is highly dependent on the material and on the geometrical design: the silicon core of the strip waveguide is surrounded by $SiO_2$ and the distance between the core and the substrate plays a crucial role since an higher thickness of $SiO_2$ is associated with lower thermal conductivity, which leads to an increase in the value of the thermal impedance $Z_T$.

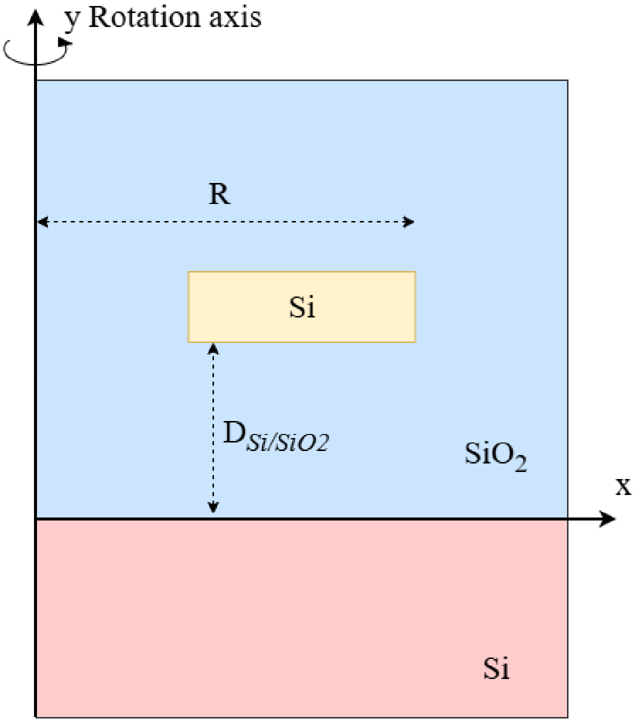

**Figure 2.7:** Cross-section of a silicon MRR.

From the design point of view, the thermal impedance decreases as the resonator length increases, since the area where heat can be dissipated is larger, allowing the structure to release heat more efficiently.

To have a better understanding of heat transfer within the MRR, the Foster model is employed. This model consists of an equivalent electrical circuit formed by a series of $n$ nodes, each represented by an RC block as shown below, where $\Delta T_i$ denotes the temperature variation at the $i$-th node. The total temperature variation over time is then given by:

$$\Delta T(t) = \sum_{i=1}^{n} \Delta T_i \left(1 - e^{\frac{t}{Z_{T,i} C_i}}\right) \tag{2.21}$$

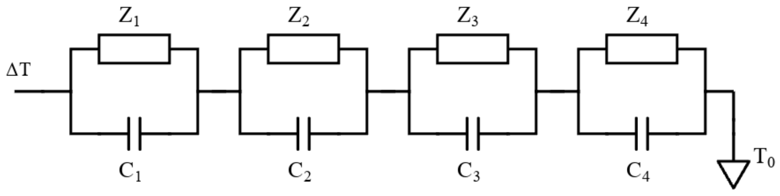

**Figure 2.8:** Foster model equivalent thermal circuit.

The thermal impedance values are obtained using the COMSOL Multiphysics thermodynamic software. The simulation of the thermal behavior consists of injecting a circulating power of 10 mW inside the ring at $t = 0$. The simulation is run until the temperature variation reaches saturation, after which the resulting transient curve is fitted. A reliable fitting cannot be achieved with a single time constant, instead, multiple nodes are required to accurately model the transient thermal response. Each node is associated with a thermal time constant and in particular every node represents a partial temperature variation $\Delta T_i$. According to Eq. (2.20) the corresponding thermal impedance $Z_{T,i}$ of each node can be determined by knowing the power absorbed in the waveguide core.

From the Foster model it is observed that each node is represented by the parallel connection of a thermal impedance $Z_T$ and a thermal capacitance $C$. The capacitance can be obtained by knowing the thermal time constant value of the node, according to the following relation:

$$\tau_{\mathrm{th},i} = Z_{T,i} C_i \tag{2.22}$$

In the table 2.1, the values of the thermal time constants, thermal impedances, and capacitances for each node, obtained from the simulation, are shown.

**Table 2.1:** Thermal parameters of the Foster model nodes.

| **Node** | $\boldsymbol{\tau_{\mathrm{th},i}}$ [s] | $\boldsymbol{Z_{T,i}}$ [Ω] | $\boldsymbol{C_i}$ [F] |
|---|---|---|---|
| 1 | $1.9253 \times 10^{-7}$ | $9.245 \times 10^{3}$ | $3.12 \times 10^{-10}$ |
| 2 | $9.246 \times 10^{-8}$ | $5.790 \times 10^{3}$ | $1.60 \times 10^{-9}$ |
| 3 | $2.4335 \times 10^{-7}$ | $3.792 \times 10^{3}$ | $1.28 \times 10^{-8}$ |
| 4 | $4.83 \times 10^{-8}$ | $1.272 \times 10^{3}$ | $1.90 \times 10^{-7}$ |

## 2.3 Overview of Nonlinear Effects in Silicon

Microring resonators exhibit non-linear effects when the power injected in the ring increases. These effects cause wavelength shifts and distortions of the ring's spectral response.

The main effects responsible for spectral distortion are two-photon absorption (TPA) and free carrier absorption (FCA). TPA occurs when the combined energy of two photons is sufficient to excite an electron from the valence band to the conduction band, creating an electron-hole pair. This mechanism generates free carriers, which can subsequently absorb additional photons through FCA, promoting carriers to higher energy levels within the conduction or valence bands. Consequently, TPA and FCA increase the overall optical loss, leading to a reduction of the resonator's quality factor and consequent distortion of the optical response.

The generated free carriers (FCs) also induce a change in the refractive index. This effect is known as Free-Carrier Dispersion (FCD), which is responsible for a shift of the ring's resonance towards shorter wavelengths. On the other hand, the relaxation (thermalization) and recombination of FCs through Shockley–Read–Hall (SRH) processes release energy in the form of heat (self-heating), leading to a temperature increase in the resonator. This thermal effect modifies the refractive index and results in a shift of the resonant wavelength towards longer wavelengths. The Kerr effect is also taken into account as it induces a slight shift towards longer wavelengths to the resonance, even if its contribution is much smaller compared to FCA and self-heating.

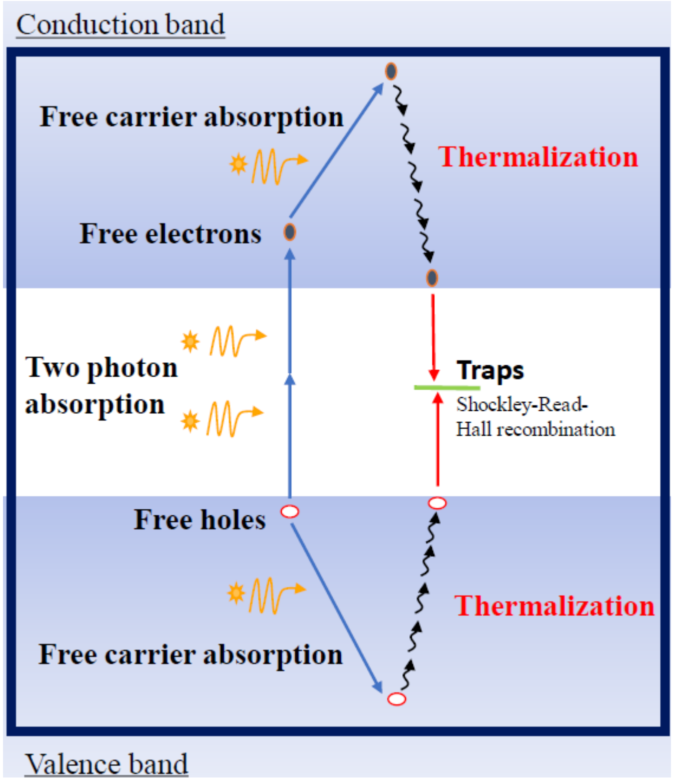

**Figure 2.9:** Schematic of the nonlinear effects in Si. Reprinted from [5].

## 2.4 Static Analysis and SRH model for carrier recombination

### 2.4.1 Phase variation

The overall phase accumulation in Eq. 2.10 is influenced by nonlinearities, thermal effects, and the Kerr effect, all accounted in the term $\Delta\theta(P_c, \Delta T)$. Consequently, the phase becomes a function of the circulating optical power, the resonator temperature, and the free carrier densities $n_e$ and $p_e$, and can be written as:

$$\theta(P_c, T, n_e, p_e) = \theta_0 + \frac{n_g}{c}(\omega - \omega_0)L + \Delta\theta(P_c, T, n_e, p_e). \tag{2.23}$$

The nonlinear term is related to the effective refractive index variation $\Delta n_{\text{eff}}(P_c, T, n_e, p_e)$ as $\Delta\theta = \frac{2\pi L}{\lambda_0}\Delta n_{\text{eff}}$.

### 2.4.2 Propagation losses

In addition to the modal losses experienced by the field during propagation in the ring, further losses must be considered because of nonlinear effects. Referring to free carriers as the carrier densities per unit volume, $n_e$ for electrons and $p_e$ for holes, these effective losses can be expressed as:

$$\alpha_{\text{eff}}(P_c, n_e, p_e) = \alpha_0 + \alpha_{\text{rad}} + \Delta\alpha(P_c, n_e, p_e), \tag{2.24}$$

with

$$\Delta\alpha(P_c, n_e, p_e) = \alpha_{\text{TPA}}(P_c) + \Delta\alpha_{\text{FCA}}(n_e, p_e). \tag{2.25}$$

The last term is related to the nonlinear losses and it is composed by $\alpha_{\text{TPA}}(P_c)$, the losses due to two-photon absorption, which depends linearly on the circulating power in the ring, as expressed by the following relation:

$$\alpha_{\text{TPA}}(P_c) = \frac{\beta_{\text{TPA}}}{A_{\text{eff}}} P_c, \tag{2.26}$$

where $\beta_{\text{TPA}}$ is the two-photon absorption coefficient and $A_{\text{eff}}$ is the effective area, a measure of the nonlinear interaction of the optical field with silicon.

The other term, $\alpha_{\text{FCA}}(n_e, p_e)$, corresponds to the losses induced by free-carrier absorption and is expressed through the following empirical expression [7]:

$$\Delta\alpha_{\text{FCA}}(n_e, p_e) = \Gamma\left(8.88 \cdot 10^{-21}\, n_e^{1.167} + 5.84 \cdot 10^{-20}\, p_e^{1.109}\right), \tag{2.27}$$

where $\Gamma$ is the mode confinement factor, $n_e$ is the electron density, and $p_e$ is the hole density, both expressed in $[cm^{-3}]$.

### 2.4.3 Refractive index variation

The total refractive index variation is the sum of different contributions, related to the free carriers and to self-heating:

$$\Delta n_{\text{eff}} = \Delta n_{\text{eff,FCD}} + \Delta n_{\text{eff,Kerr}} + \Delta n_{\text{eff,T}}, \tag{2.28}$$

where $\Delta n_{\text{eff,FCD}}$ is the variation due to free-carrier dispersion (FCD), $\Delta n_{\text{eff,Kerr}}$ is the variation induced by the Kerr effect and $\Delta n_{\text{eff,T}}$ is the contribution related to thermalization and consequent self-heating of the ring.

The FCD contribution is given by the following empirical relation [7]:

$$\Delta n_{\text{eff,FCD}} = -\Gamma\left(5.4 \cdot 10^{-22}\, n_e^{1.011} + 1.53 \cdot 10^{-18}\, p_e^{0.838}\right), \tag{2.29}$$

The contribution due to the Kerr effect (SPM) can be expressed as:

$$\Delta n_{\mathrm{eff,Kerr}} = \Gamma n_2 \frac{P_c}{A_{\mathrm{eff}}}, \tag{2.30}$$

where $n_2$ is the Kerr coefficient in silicon.

### Thermal dispersion

For the refractive index variation due to self-heating, it is necessary to quantify the power absorbed by the ring, that is the fraction of optical power converted into heat. This absorbed power is a function of the circulating power and it is expressed as:

$$P_{\mathrm{abs}} = P_c \left(1 - a_{\mathrm{abs}}\right) \left(1 + t^2 \cdot a\right), \tag{2.31}$$

where

$$a_{\mathrm{abs}} = e^{-(\alpha_0 + \Delta\alpha(P_c)) \cdot L/2}. \tag{2.32}$$

So the absorbed power originates from linear propagation loss, two-photon absorption (TPA), and free-carrier absorption (FCA), and is converted into heat in the silicon core.

The circulating power therefore determines the amount of absorbed power, which is used as the input of the RC thermal network to calculate the temperature variation at the different nodes:

$$\frac{dT_i}{dt} = -\frac{T_i}{\tau_i} + \frac{P_{abs}}{C_i}, \qquad i = 1, \ldots, 4, \tag{2.33}$$

After evaluating the total temperature variation as the sum of the contributions of each node as:

$$\Delta T = \sum_i \Delta T_i. \tag{2.34}$$

we obtain the effective refractive index change due to self-heating:

$$\Delta n_{\mathrm{eff},T} = \Gamma \frac{dn_{Si}}{dT} \Delta T_{\mathrm{tot}}, \tag{2.35}$$

where $\frac{dn_{Si}}{dT}$ is the silicon thermo-optic coefficient.

### 2.4.4 Differential equations for free carriers density

Since the nonlinear effects depend mainly on the free carrier density as can be seen from 2.27 and 2.29, this subsection focuses on the differential equations that describes the generation and the dynamics of free carriers.

The rate equation for free carriers is in the following form:

$$\frac{dN}{dt} = G_{\text{gen}} - R_{\text{rec}}, \tag{2.36}$$

where $G_{\text{gen}}$ is the carrier generation rate, which will be discussed later, and $R_{\text{rec}}$ is the total recombination rate.

In the case of silicon microring resonators, the only recombination mechanism is non-radiative and it is the Shockley–Read–Hall (SRH) recombination: free carriers are captured by defects or impurities within the crystal lattice, which act as traps. Electrons and holes then recombine through the energy levels associated with these traps, releasing energy in the form of heat.

The time evolution of the excess carrier densities in the semiconductor can be described by the following Shockley–Read–Hall (SRH) rate equations [**ref9**]:

$$\frac{dn_e}{dt} = G - \frac{1}{\tau_{n0}} \left[ \frac{(n_0 + n_1 + n_e)(n_e - p_e)}{N_f} + \frac{n_e n_1}{n_0 + n_1} \right], \tag{2.37}$$

$$\frac{dp_e}{dt} = G - \frac{1}{\tau_{p0}} \left[ \frac{(p_0 + p_1 + p_e)(p_e - n_e)}{N_f} + \frac{p_e p_1}{p_0 + p_1} \right], \tag{2.38}$$

where:

- $n_e$ and $p_e$ are the excess electron and hole densities, respectively,
- $n_0$ and $n_1$ are the electron concentrations under equilibrium conditions,
- $p_0$ and $p_1$ are the hole concentrations under equilibrium conditions,
- $N_f$ is the trap density,
- $\tau_{n0}$ and $\tau_{p0}$ are the recombination lifetimes for electrons and holes, respectively.

In both equations, the first term represents the carrier generation rate $G$, while the second term represents SRH recombination through traps.

For the total SRH generation rate $G$, both carriers generated by Two-Photon Absorption (TPA) and Surface-Charge Absorption (SCA) must be taken into account. SCA consists of the absorption of a single photon that promotes an electron from an intra-gap state located at defects near the waveguide. Usually this contribution can be neglected.

The total generation rate can be expressed as:

$$G = \frac{\alpha_0\, \eta_{\text{SCA}}\, P_c}{\hbar\omega_0\, A\, A_{\text{eff}}} + \frac{\alpha_{\text{TPA}} P_c^2}{2\hbar\omega_0 A}, \tag{2.39}$$

where $\eta_{\text{SCA}}$ is the SCA efficiency, $\hbar\omega_0$ is the photon energy, $A$ is the waveguide cross-sectional area.

### 2.4.5 Pump-probe differential equations

In the pump–probe experiment, two signals are injected into the MRR, corresponding to the pump and probe fields, at two different wavelengths set at two adjacent resonances, $\lambda_{0,1}$ and $\lambda_{0,2}$ of the MRR. The pump signal, at high power, is responsible for inducing nonlinear effects in the ring through the generation of a large number of free carriers, while the probe signal, at low power, is used to monitor the dynamics of the ring and the effects induced by the pump signal.

In this subsection, the field equations for the pump and probe signals are analyzed with the effects coming from the interaction of the two fields on the nonlinearities of the MRR.

Therefore, two circulating fields are present in the ring, defined as:

$$E_{\text{ring},1}(t) = E_{c,1}(t)\, e^{-j\omega_{0,1}t}, \qquad E_{\text{ring},2}(t) = E_{c,2}(t)\, e^{-j\omega_{0,2}t}. \tag{2.40}$$

The differential equations for the circulating fields of the pump and probe signals are:

$$\begin{aligned} \frac{\partial E_{c,1}}{\partial t} &= -\frac{1}{\tau_{g,1}}\left(\frac{\kappa_1\sqrt{1-\eta^2}}{t_1^2\, a_1(t)}\, E_{\text{bus},1} + E_{c,1}(t)\left(\frac{1}{t_1^2 a_1(t)} - 1\right)\right. \\ &\quad \left. + j\left(\frac{L}{c}\Delta\omega_{r,1}(t) + \tau_{g,1}\delta\omega_1\right) E_{c,1}(t)\right). \end{aligned} \tag{2.41}$$

$$\begin{aligned} \frac{\partial E_{c,2}}{\partial t} &= -\frac{1}{\tau_{g,2}}\left(\frac{\kappa_2\sqrt{1-\eta_2^2}}{t_2^2\, a_2(t)}\, E_{\text{bus},2} + E_{c,2}(t)\left(\frac{1}{t_2^2 a_2(t)} - 1\right)\right. \\ &\quad \left. + j\left(\frac{L}{c}\Delta\omega_{r,2}(t) + \tau_{g,2}\delta\omega_2\right) E_{c,2}(t)\right). \end{aligned} \tag{2.42}$$

With $P_{\text{bus},1,2} = |E_{\text{bus},1,2}|^2$, $P_{c,1,2} = |E_{c,1,2}|^2$, $\Delta\omega_{r,1,2} = \omega_{0,1,2} \cdot \Delta n_{\text{eff},1,2}$, and $\tau_{g,1,2} = L \cdot n_{g,1,2}/c$. Here, $\delta\omega_{1,2}$ is the pump and probe detuning with respect to the cold resonances. Usually in the pump-probe experiment the pump detuning is set to zero in order to maximize the circulating field and hence carrier generation, while on the other hand the probe can be detuned around $\lambda_{0,2}$ depending on the application.

Regarding the thermal response, since two fields are present, two absorbed powers must be considered. Therefore, 2.33 is evaluated separately for the pump and probe fields:

$$\begin{aligned} \frac{dT_i^{(1)}}{dt} &= -\frac{T_i^{(1)}}{\tau_i} + \frac{P_{\text{abs},1}}{C_i}, \\ \frac{dT_i^{(2)}}{dt} &= -\frac{T_i^{(2)}}{\tau_i} + \frac{P_{\text{abs},2}}{C_i}, \end{aligned} \qquad i = 1, \ldots, 4. \tag{2.43}$$

The total temperature variation is then obtained as the sum of the contributions from both fields:

$$\Delta T_i(t) = T_i^{(1)}(t) + T_i^{(2)}(t), \qquad i = 1, \ldots, 4. \tag{2.44}$$

Finally the refractive index variation due to self heating in the pump-probe experiment is computed as:

$$\Delta n_{\text{eff},T}^{(1,2)} = \Gamma_{1,2} \frac{dn_{\text{Si}}}{dT} \Delta T_{\text{tot}} \tag{2.45}$$

where $\Gamma_{1,2}$ are the confinement factor respectively of the pump and probe fields.

For what regards the pump-probe experiment, additional terms for the nonlinear effects induced in the MRR dyamic must be taken into account. With two different signals of pump and probe, the absorption of one photon from the pump together with one photon from the probe leads to additional effective losses, known as cross Two-Photon Absorption (XTPA). Similarly, the probe and pump fields induce reciprocal phase variations through the Kerr effect, a mechanism referred to as cross-phase modulation (XPM).

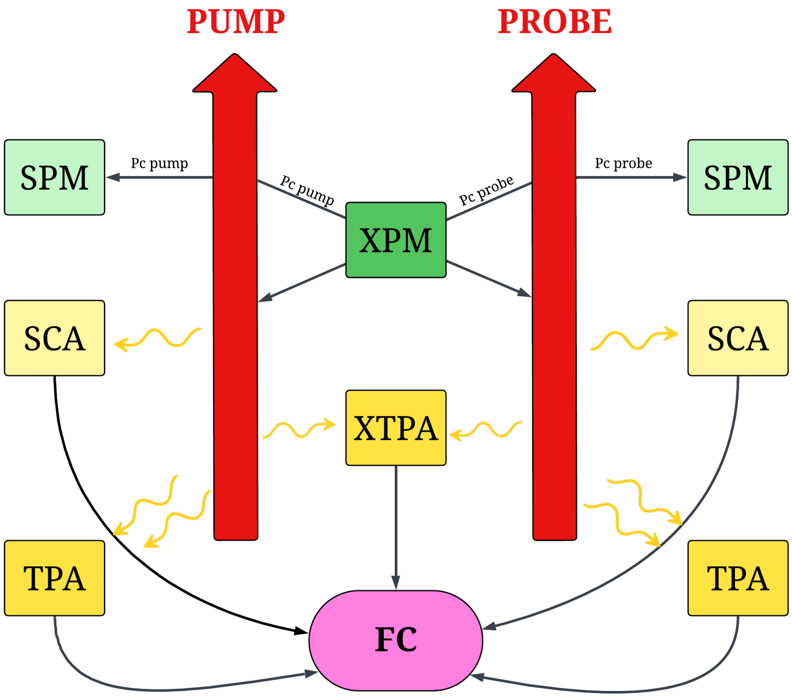

**Figure 2.10:** Schematic overview of the nonlinear effects in the pump-probe experiment.

These nonlinear interactions are therefore included in the formulation of the pump-probe effective losses $\alpha_{\mathrm{eff},1/2}(t)$ and the carrier generation rate $G(t)$.

For the pump field, the effective losses are given by:

$$\alpha_{\mathrm{eff},1} = \alpha_0 + \frac{\beta_{\mathrm{TPA}}}{A_{\mathrm{eff},1}} P_{c,1} + 2\,\frac{\beta_{\mathrm{TPA}}}{A_{\mathrm{eff,av}}} P_{c,2} + \Gamma_1 \Delta\alpha_{\mathrm{FCA}}, \tag{2.46}$$

while for the probe field:

$$\alpha_{\mathrm{eff},2} = \alpha_0 + \frac{\beta_{\mathrm{TPA}}}{A_{\mathrm{eff},2}} P_{c,2} + 2\,\frac{\beta_{\mathrm{TPA}}}{A_{\mathrm{eff,av}}} P_{c,1} + \Gamma_2 \Delta\alpha_{\mathrm{FCA}}, \tag{2.47}$$

where $A_{\mathrm{eff,av}} = \sqrt{A_{\mathrm{eff},1}\, A_{\mathrm{eff},2}}$.

The total free carrier generation rate, including XTPA, can be expressed as:

$$\begin{aligned} G = G_{\mathrm{SCA},1} &+ \frac{\beta_{\mathrm{TPA}} P_{c,1}^2}{2\hbar\omega_{0,1} A A_{\mathrm{eff},1}} + \frac{\beta_{\mathrm{TPA}} P_{c,2}^2}{2\hbar\omega_{0,2} A A_{\mathrm{eff},2}} \\ &+ \frac{\beta_{\mathrm{TPA}} P_{c,1} P_{c,2}}{\hbar\omega_{0,1} A A_{\mathrm{eff,av}}} + \frac{\beta_{\mathrm{TPA}} P_{c,1} P_{c,2}}{\hbar\omega_{0,2} A A_{\mathrm{eff,av}}}. \end{aligned} \tag{2.48}$$

The first three terms correspond to the SCA and TPA contributions from the pump and probe, the last two terms represent the generation of free carriers due to cross Two-Photon Absorption (XTPA) between the pump and probe fields.

Finally, the pump and probe fields also interact through the cross-phase modulation (XPM) effect, which adds to the self-phase modulation (SPM):

$$\Delta n^{(1,2)}_{\mathrm{eff,Kerr}} = \Gamma_{1,2} n_2 \left( \frac{P_{c,1,2}}{A_{\mathrm{eff},1,2}} + 2\frac{P_{c,2,1}}{A_{\mathrm{eff,av}}} \right). \tag{2.49}$$

## 2.5 Si-PolySi Ring Modelling

The case of interest of this work consists of a waveguide composed of two slabs, silicon and polysilicon, stacked on top of each other.

For materials different from crystalline silicon, such as polysilicon, the optical confinement factors $\Gamma_{\mathrm{Si}}$ and $\Gamma_{\text{poly-Si}}$ are introduced to weight the contribution of the two waveguides to the propagating field. This type of waveguide allows the field to be confined almost equally in both silicon and polysilicon, resulting in very similar confinement factors. The effective FCA losses can be expressed as:

$$\Delta\alpha_{\mathrm{FCA,exp}}(t) = \Gamma_{\mathrm{Si}}\, \Delta\alpha_{\mathrm{FCA,exp,Si}}(t) + \Gamma_{\text{poly-Si}}\, \Delta\alpha_{\text{FCA,exp,poly-Si}}(t). \tag{2.50}$$

Similarly, for the refractive index variation due to free-carrier dispersion (FCD), we can write:

$$\Delta n_{\text{eff,FCD,exp}}(t) = \Gamma_{\text{Si}}\, \Delta n_{\text{eff,FCD,exp,Si}}(t) + \Gamma_{\text{poly-Si}}\, \Delta n_{\text{eff,FCD,exp,poly-Si}}(t). \tag{2.51}$$

Here, $\Delta\alpha_{\text{FCA,exp,Si}}(t)$ and $\Delta\alpha_{\text{FCA,exp,poly-Si}}(t)$ represent the FCA losses in the silicon and polysilicon waveguides, respectively, while $\Delta n_{\text{eff,FCD,exp,Si}}(t)$ and $\Delta n_{\text{eff,FCD,exp,poly-Si}}(t)$ represent the variation of the refractive index due to FCD in the two waveguides.

In polysilicon, the FCA can be expressed as:

$$\Delta\alpha_{\text{FCA,poly}} = \Gamma_{\text{poly-Si}} \left(5.2 \times 10^{-20}\, n_e^{1.167} + 1.2 \times 10^{-19}\, p_e^{1.109}\right), \tag{2.52}$$

and the corresponding refractive index variation due to FCD is:

$$\Delta n_{\text{eff,FCD,poly}} = -\Gamma_{\text{poly-Si}} \left(6.6 \times 10^{-22}\, n_e^{1.011} + 2.4 \times 10^{-18}\, p_e^{0.838}\right). \tag{2.53}$$

Polysilicon is characterized by the presence of defects within its crystalline grains, which act as recombination centers for free carriers. The grain size and the large number of grain boundaries strongly affect carrier mobility, trap density, and thermal conductivity. As a consequence of these defects, polysilicon typically exhibits larger linear losses. Furthermore, polysilicon experiences stronger FCA compared to crystalline silicon; however, the same defects also dramatically reduce the free-carrier lifetimes, leading to a consequently reduced impact of FCA.

# Chapter 3

# Characterization of the Si PolySi microring resonator

In this chapter will be discussed the characterization of the silicon and polysilicon microring resonator selected for the pump and probe experiment. Steady-state measurements of the transmission coefficient of the MRR have been performed both in the linear regime, in order to perform a fitting and extract the characteristic parameters of the ring, and in the non linear regime where the effects described in Chapter 2 are observed.

## 3.1 Si-PolySi ring resonator

The Si–PolySi ring resonator under test is based on the SISCAP platform [8], where the ring waveguide consists of a rectangular undoped polysilicon core placed on top of a silicon core, as shown in Figure 3.1. The ring configuration features a single input waveguide that also functions as a drop port, connected through an optical splitter, and two through ports. The main geometrical dimensions of the ring resonator are reported in Table 3.1.

**Table 3.1:** Geometrical parameters of the Si and PolySi ring resonator.

| **Parameter** | **Ring Si/PolySi** | | **Unit** |
|---|---|---|---|
| | **Si** | **PolySi** | |
| *Radius* | 2 | | µ*m* |
| *W* | 400 | 400 | *nm* |
| *h* | 115 | 125 | *nm* |

The coupling technique used is an edge coupling technique adopted with a Spot Size Converter (SSC). Table 3.2 reports the values of the splitter and the coupling losses at the input and output for both ports 1 and 2. The input coupling losses were measured using an optical circulator. Once the input losses were estimated, the output coupling losses were derived by measuring the insertion loss of the ring with the laser wavelength set outside the resonance condition.

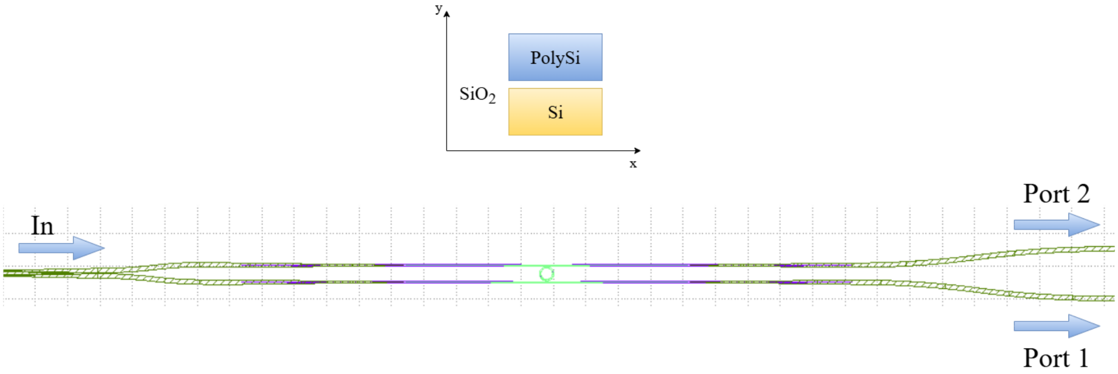

**Figure 3.1:** Structure and configuration of the Si-PolySi MRR under test.

**Table 3.2:** Measured coupling losses and splitter ratio for the Si-PolySi ring resonator.

| Parameter | Value | Unit |
|---|---|---|
| Coupling losses input | 2.5 | dB |
| Coupling losses output Port 1 | 7.5 | dB |
| Coupling losses output Port 2 | 6.0 | dB |
| Splitter ratio | 0.5 | – |

As can be observed, port 2 exhibits lower coupling losses compared to port 1. For this reason, in the pump and probe experiment, port 2 is used as the output of the ring.

Figure 3.2 shows the fitting of the measured bend losses for a Si-PolySi ring with a radius of 2 $\mu m$. These extracted values are implemented in the model to estimate the radiative losses $\alpha_{\text{rad}}$.

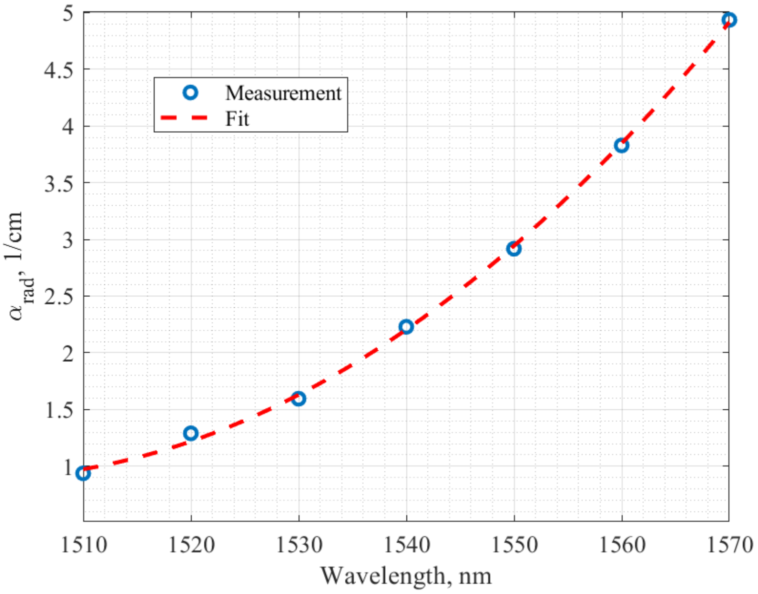

**Figure 3.2:** Measurement and fitting of bend losses for a Si-PolySi MRR with $2\mu m$ radius.

## 3.2 Steady state set up

In order to perform the steady state measurements in both the linear and non linear conditions the optical power is injected into the bus waveguide from a tunable laser (Hewlett Packard 8168F). In order to reach high power level, for the non linear measurements, the optical signal is amplified by means of an Erbium-Doped Fiber Amplifier (EDFA) followed by an optical filter (JDS TB9 Optical Grating Filter) to reduce the residual Amplified Spontaneous Emission (ASE). Before coupling into the ring, a polarization controller (PC) is also employed to ensure that the incident light on the SSCs is TE polarized, as the converters are designed to operate only for this polarization. The transmission coefficient measurements of the Si-PolySi MRRs are strongly polarization dependent. For this reason, the polarization controller is adjusted in order to have the output power from the ring symmetric on both sides of the resonance.

The tunable laser wavelength is then swept around the resonant wavelength of the ring, $\lambda_{0,1}$. The transmission coefficient at the through port is obtained as the ratio between the input power and the output power at the through port, measured using an optical power meter.

The fiber-to-chip alignment is achieved by means of a 6-degree mechanical stage positioning system with a precision of ±0.06 $\mu$m. The chip is mounted on a Peltier cell, with the temperature stabilized at 25°C using a Thermo Electric Cooler (TEC) controller.

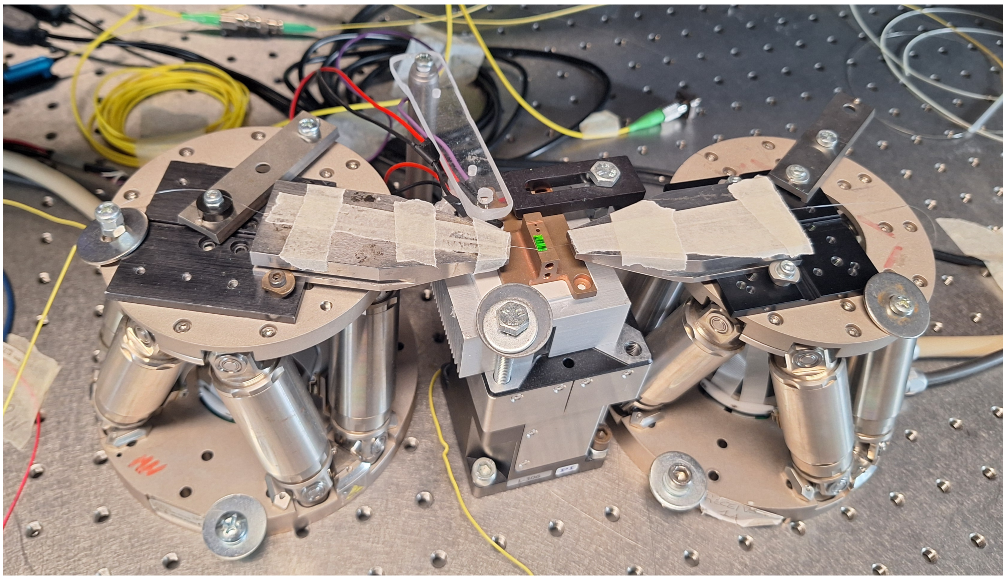

**Figure 3.3:** Laboratory setup: the chip is mounted on a Peltier cell, with two hexapod, used to align precisely the fiber at the input and at the output of the chip.

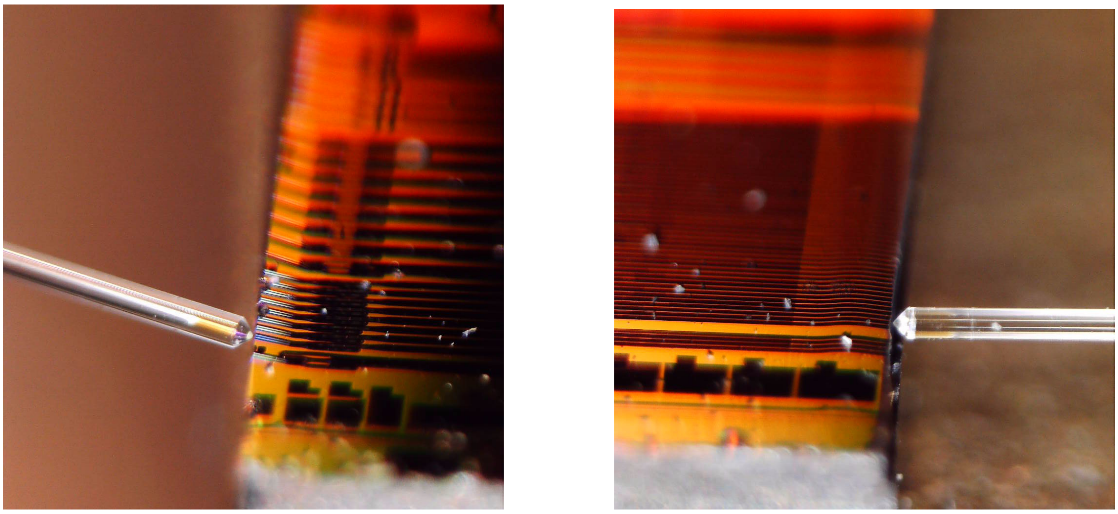

**(a)** Input fiber coupling **(b)** Output fiber coupling

**Figure 3.4:** Fiber coupling at the input and output of the chip.

## 3.3 Linear regime measurements and fitting

The following section aims to extract the characteristic parameters of the MRR in order to identify the ring suitable for the pump and probe experiment.

After identifying two adjacent resonances by means of an Optical Spectrum Analyzer (OSA), measurements in the linear regime are carried out by setting the tunable laser power at 10 $\mu$W in order to inject in the MRR low power to avoid the occurrence of non linear effects in both silicon and polysilicon. Then the wavelength sweep is performed and the transmission coefficient for both resonances is measured at ports 1 and 2 of the MRR. The measured spectra with their corresponding fittings are reported below.

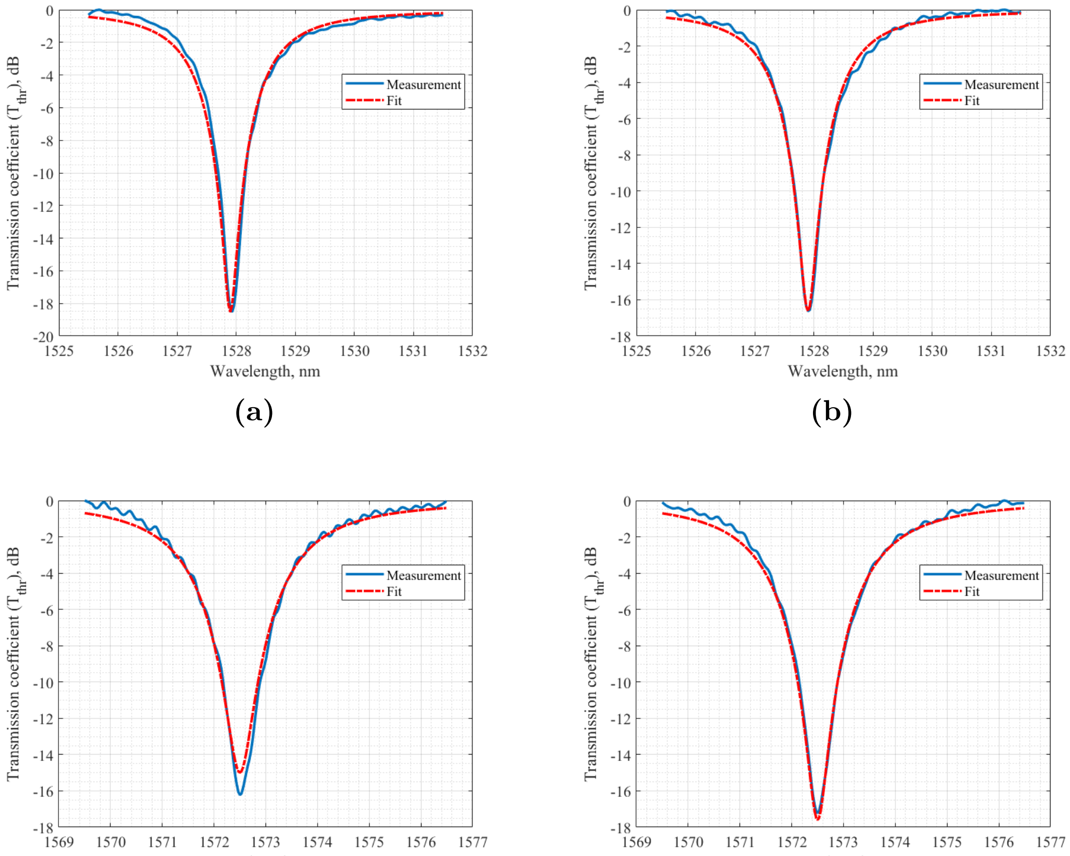

**(a)** **(b)**

**(c)** **(d)**

**Figure 3.5:** Measured transmission coefficients and fittings of the MRR at two resonances.(a) and (b) are port1 and port 2 at the first resonance, (c) and (d) are port 1 and port 2 at the second resonance.

The fitting is performed by fixing certain parameters, such as the intrinsic losses $\alpha_0$, the coupling-related losses $\eta$, and the group index $n_g$. Since port 2 present the best fit and lower output coupling losses, as previously explained, it is therefore preferred for the pump and probe experiment. Extracted parameters are in the table 3.3. In the fitting procedure optical refractive index $n_{eff}$ for PolySi is assumed to be the same as for Si.

**Table 3.3:** Extracted parameters of the Si-PolySi MRR at port 2.

| **Parameter** | **Pump** | | **Probe** | | **Unit** |
|---|---|---|---|---|---|
| | **Si** | **PolySi** | **Si** | **PolySi** | |
| $\lambda_{\text{res}}$ | 1527.9 | | 1572.5 | | $nm$ |
| $Q$ | 1015 | | 680 | | – |
| $\kappa^2$ | 0.1177 | | 0.1751 | | – |
| $\alpha_0$ | 1.02 | 8 | 1.02 | 8 | $dB/cm$ |
| $\eta^2$ | 0.004 | | 0.004 | | – |
| $n_g$ | 4.2 | | 4.2 | | – |
| $\alpha_{\text{rad}}$ | 1.53 | | 5.2 | | $dB/cm$ |
| $n_{\text{eff}}$ | 2.34 | | 2.25 | | – |
| $\Gamma$ | 0.50 | 0.50 | 0.46 | 0.51 | – |
| $A_eff$ | 0.140 | 0.165 | 0.177 | 0.159 | $\mu m^2$ |

It is important to note that, in general, the Si-PolySi ring exhibits a quality factor $Q$ that is significantly lower than the one of a silicon ring, as can be seen in Figure 3.6, which shows the fitting of a linear measurement for a silicon ring. This implies that, for the same circulating power in the MRR, the non linear effects observed in a silicon ring are expected to be stronger than those in the Si-PolySi ring.

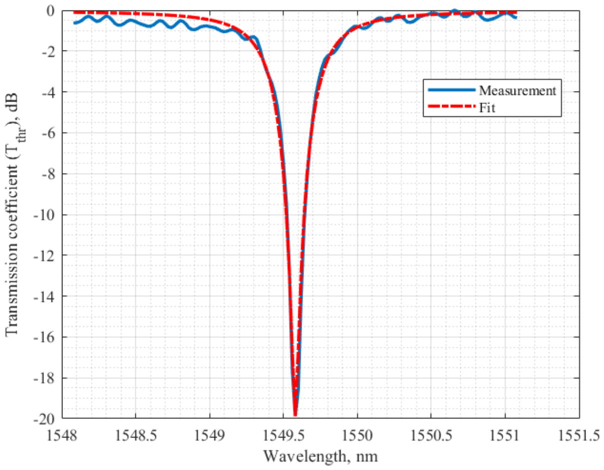

**Figure 3.6:** Measured transmission coefficient and fitting of a pure silicon MRR: the quality factor extracted from the fitting is 4145.

## 3.4 Non linear regime measurements

After extracting the main figures of merit of the MRR, the behavior of the transmission coefficient is analyzed as a function of the input power. The measurements are performed following the same procedure as in the linear regime, with the addition of an EDFA, followed by the optical filter, to amplify the optical signal and achieve power levels sufficient to trigger non linear effects in both silicon and polysilicon.

The bus power ($P_{bus}$) for each transmission coefficient measurement is estimated by measuring the non-normalized transmission coefficient at both sides of the resonance, performing a linear fitting, and evaluating the corresponding power value at the resonance wavelength of the curve. The output coupling losses are then added to obtain the total bus power.

Initially, non linear measurements were performed on a Si ring resonator (figure 3.7), from which the resonance shift and the transmission coefficient variation as a function of the input power were extracted, as shown in figure 3.8.

Subsequently, the same type of measurement was performed on the Si-PolySi ring resonator. In this case, the measurements are focused on the resonance at 1527.9 nm, referred to as the pump. Figure 3.9 shows the nonlinear measurements, while Figure 3.10 reports the corresponding resonance shift and transmission coefficient.

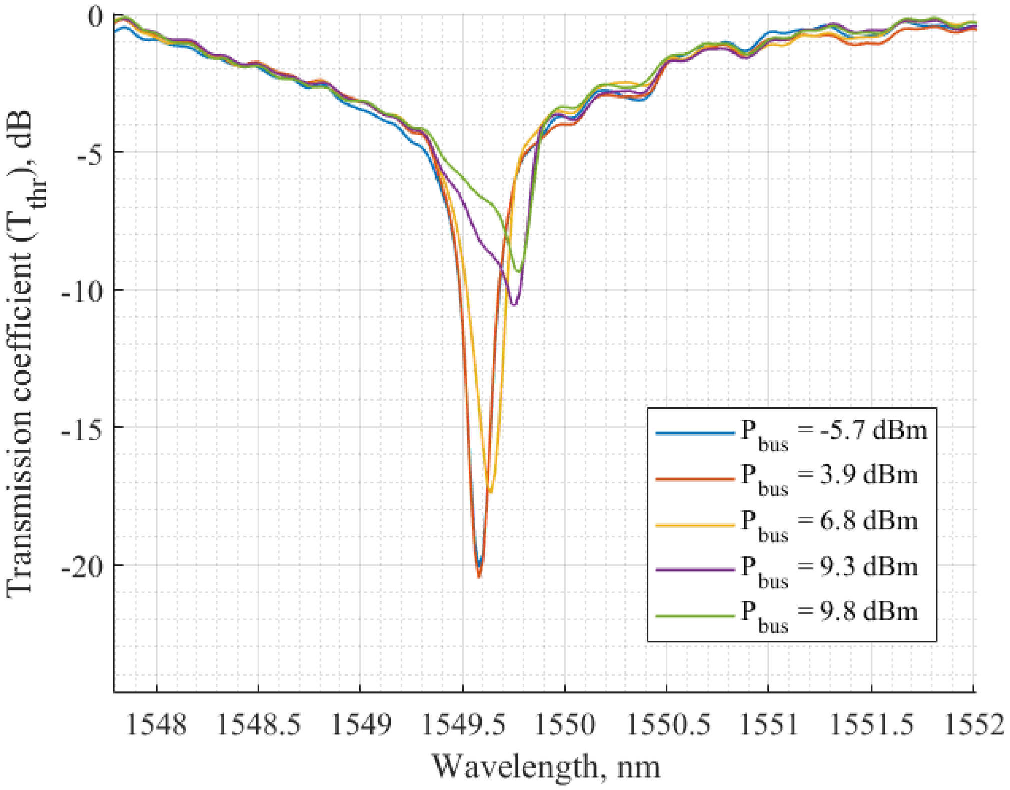

**Figure 3.7:** Non linear measurements performed on a Si MRR.

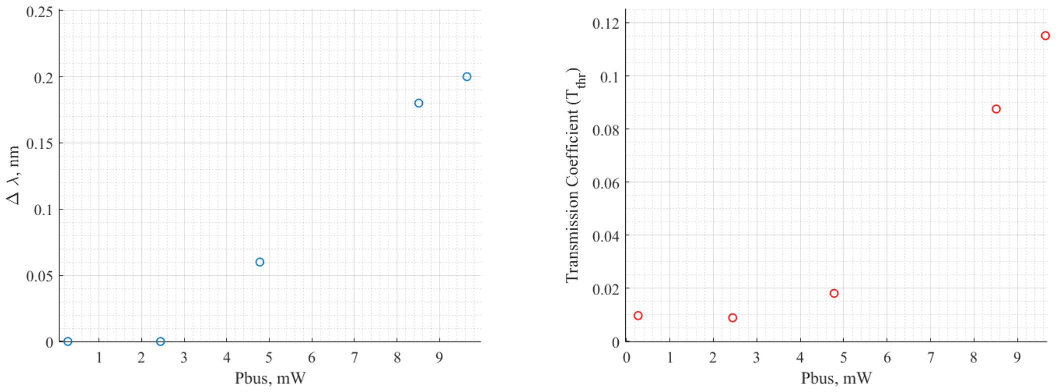

**(a)** Resonance wavelength shift. **(b)** Transmission shift at the through port.

**Figure 3.8:** Extracted resonance wavelength shift (a) and the transmission coefficient variation (b) for the Si ring resonator.

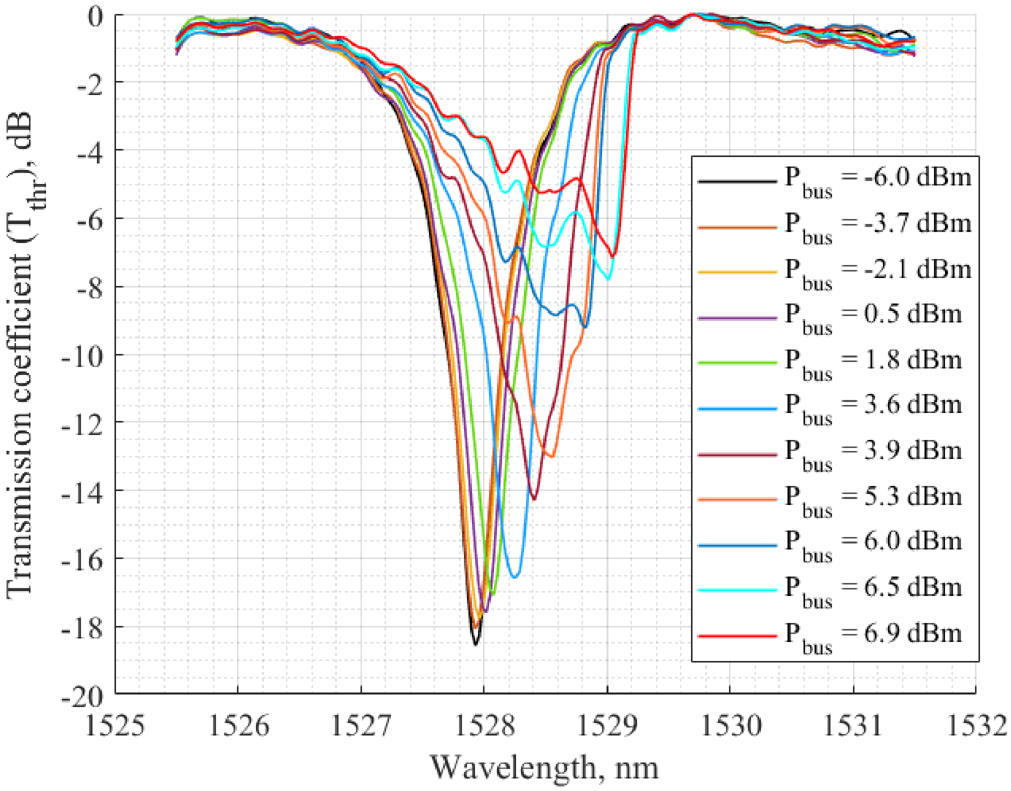

**Figure 3.9:** Measurements of the Si-PolySi MRR transmission oefficient varying the input power.

Let's focus on the Si-PolySi case: up to a bus power of $P_{\text{bus}} = -6$ dBm, the spectrum corresponds to the linear response. As the power increase, non linear effects start to appear: the quality factor of the transmission spectrum degrades due to the rise of optical losses caused by the high number of free carriers. Under continuous-wave (CW) injection, the resonance shift towards shorter wavelengths (blue shift) due to free-carrier dispersion (FCD) is not observed, since in this condition the thermal effect dominates, resulting only in a measurable shift towards longer wavelengths (red shift). This behavior is attributed to the higher thermal impedance of the Si/Poly-Si ring. In fact, in other works [3], where measurements were carried out on pure silicon rings, an initial blue shift is observed, caused by the variation of the refractive index due to FCD being dominant over the thermal effect.

For high values of $P_{\text{bus}}$, starting from 6 dBm, we can observe a sharp increase of the transmission coefficient. This is a consequence of the ring entering the bistability region, which results in a transmission spectrum characterized by a hysteresis that depends on the direction of the wavelength sweep, i.e., from low to high wavelength or from high to low wavelength.

As anticipated, from the non linear measurements, the data regarding the resonance shift $\Delta\lambda$, defined as the difference between the measured wavelength resonance $\lambda_{res}$ and the cold resonance $\lambda_0$, and the variation of the transmission coefficient were collected.

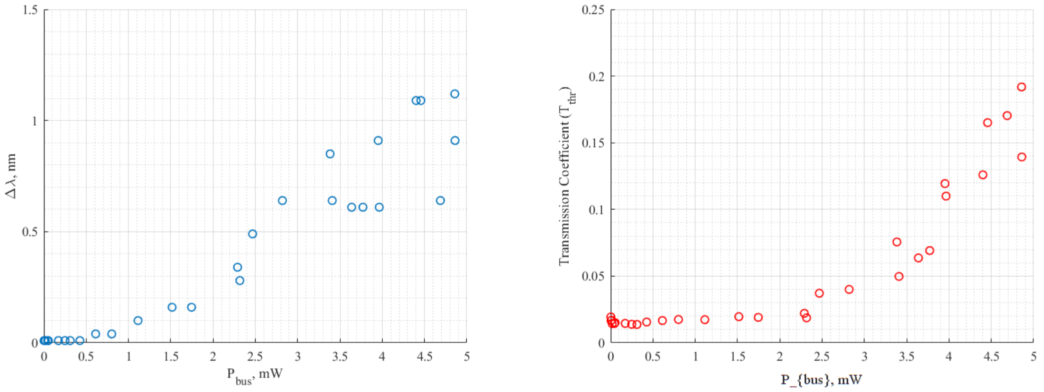

**(a)** Resonance shift **(b)** Threshold transmission shift

**Figure 3.10:** Comparison of resonance shift and threshold transmission shift.

From the resonance shift graph, a discrepancy between the expected and the measured values can be observed at higher input power. This is due to the fact that the MRR enters, for many input wavelengths, a self-oscillating regime in which a well-defined transmission spectrum cannot be obtained. For wavelengths injected around the resonance and with sufficient input power, the optical power measured at the through port oscillates over time; however, the optical power meter records only the average value of this oscillating signal. In this scenario, the ring does not operate effectively, and the measured transmission cannot be considered a reliable metric for quantifying its static non linear response.

## 3.4.1 Self-Oscillation Regime

In some specific conditions, involving a particular input wavelength and a given level of injected power in continuous-wave regime, the microring resonator can enter a self-oscillation regime. This condition is characterized by periodic oscillations of the resonant wavelength. During these oscillations, the optical power circulating within the ring becomes sufficiently high that the free-carrier lifetime becomes comparable to the thermal time constant of the resonator reported in 2.1.

To better understand the behavior of this condition, the process can be divided into four main steps.

At first, when the optical signal is aligned with the cold resonance wavelength $\lambda_0$, the circulating power inside the ring increases significantly. This results in intense free-carrier generation, which induces a shift of the resonance towards shorter wavelengths due to free-carrier dispersion. At this point, the signal becomes detuned from the cold resonance, causing a rapid decrease in circulating power. Meanwhile, the heat generated by free-carrier absorption leads to a shift of the resonance towards longer wavelengths, gradually restoring the alignment between the signal and the cold resonance. As this occurs, both FCD and self-heating effects becomes more evident because the circulating power increases again as the detuned resonance approaches its initial wavelength. However, when the resonance returns to its initial position, the maximum achievable circulating power is reduced compared to the initial condition, since the quality factor has been degraded by the high density of free carriers. The absorbed carriers generate additional heat, further shifting the resonance towards longer wavelengths and decreasing the circulating power. At the end of the process, as heat dissipates, the ring gradually cools down and returns to its initial state. This continuous sequence of carrier generation, absorption, and thermal recovery results in periodic self-oscillations of the resonance wavelength.

As anticipated in section 3.4 to detect the self-oscillations, the output signal from the through port is monitored using an optical receiver and an oscilloscope with bandwidth of 300 MHz. In order to detect the self-oscillations, the analysis was first carried out on the measured transmission spectrum for input power levels corresponding to a resonance shift equal to some of the outcome values reported in Fig. 3.10a.

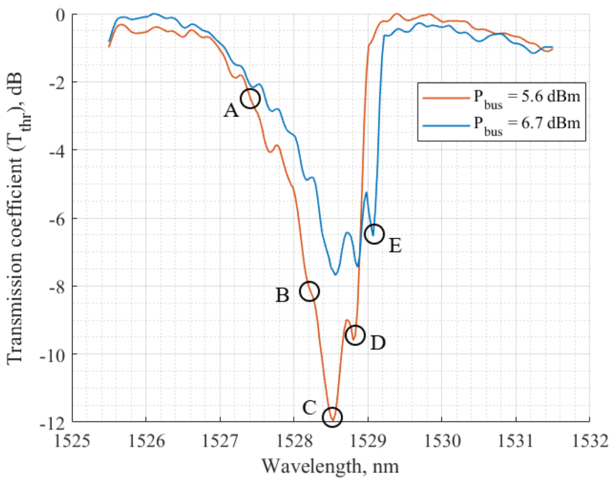

**Figure 3.11:** Transmission spectra corresponding to the outcome values of the resonance shift.

The analysis continues by setting the input power equal to the one used for the transmission spectra shown above, and tuning the signal wavelength to the points highlighted in the figure 3.11. Using the APD and the oscilloscope, the following traces in figure 3.12 are obtained. It can be observed that the fluctuations occur on the millisecond timescale and become more pronounced for $P_{bus}$ above 5.6 dBm, especially when the signal wavelength is set closer to the cold resonance value. At higher power levels, the ring operates in a fully oscillating regime, as shown in figure 3.13.

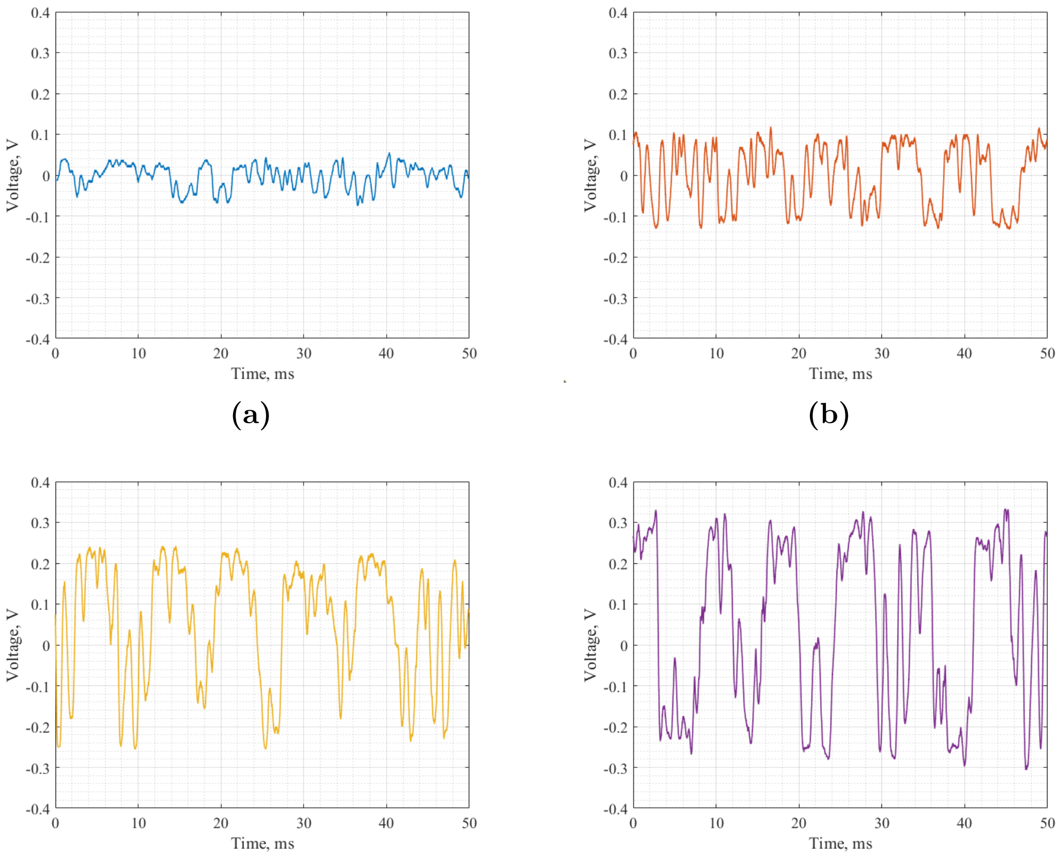

**(a)** **(b)**

**(c)** **(d)**

**Figure 3.12:** Comparison of self-oscillation cases (a)–(d).

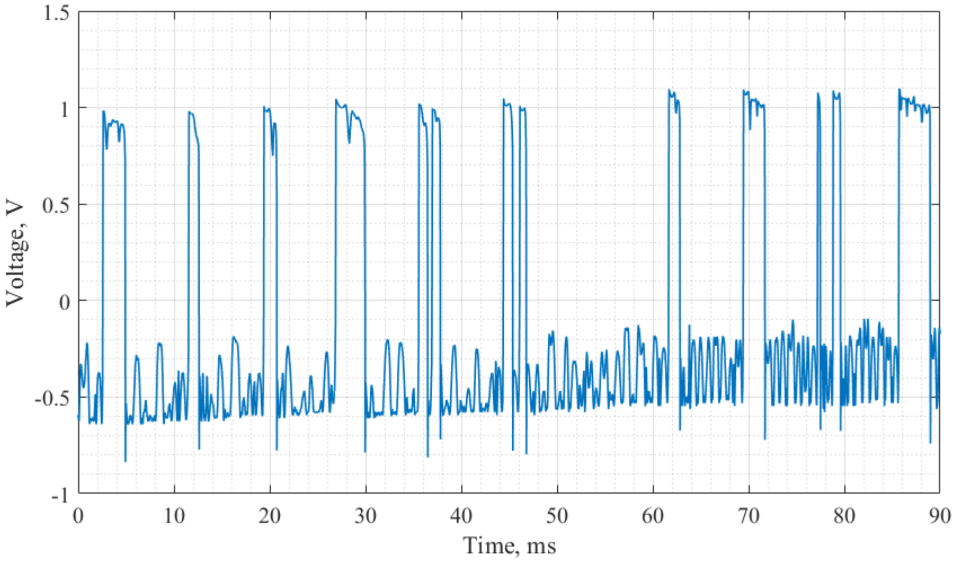

**Figure 3.13:** Full oscillating regime for $Pbus = 6.7dBm$

# Chapter 4

# Pump and probe experiment

This chapter focuses on the pump and probe experiment and its application to the Si-PolySi microring resonator [9]. A set of dynamic measurements is presented and compared with simulations obtained from the theoretical model in order to validate it. The first set of measurements were carried out with single pulses of different durations. Afterwards, the experiment was extended to the case of a binary sequence. The analysis of the model simulations allows the identification and quantification of the different dynamic effects previously introduced.

### 4.0.1 Pump and probe experimental set up

In order to perform a pump and probe experiment, two different continuous-wave (CW) tunable lasers are employed: a probe laser (Hewlett Packard 8168F) and a pump laser (Agilent N7714A Multiport). The pump and probe wavelengths are tuned to adjacent ring resonances separated by one free spectral range (FSR), namely $\lambda_{0,\text{pump}}$ and $\lambda_{0,\text{probe}}$.

The high-power CW pump signal is first modulated by a Mach–Zehnder interferometer (JDS Uniphase N-334711A), and then amplified by an erbium-doped fiber amplifier (EDFA) to achieve high peak power pulses. A waveform generator (Anritsu WFG, bandwidth = 40 GHz) allows the generation of pump pulses with periods as short as 100 ps. Meanwhile, the CW probe power in the bus waveguide is kept low to avoid any nonlinear effects or self-heating induced by the probe.

Filter 1 (JDS TB9 Optical Grating Filter), an optical grating filter centered at the pump wavelength, is used to suppress the amplified spontaneous emission (ASE) produced by the EDFA. The two signals are then coupled with a 50:50 coupler, instead of the 90:10 splitter used in other works [2, 3], since the ring exhibits higher coupling losses at both the input and output ports. For this reason, when using the 90:10 splitter, the signal detected by the APD was too weak to be measured reliably.

Since We can observe from Table 3.3 that the quality factor ($Q$) of the MRR decreases as the resonance wavelength increases, due to dispersion effects. Since a higher quality factor leads to stronger optical field enhancement, resulting in increased circulating power, higher free-carrier generation, and enhanced nonlinear effects, in the context of the pump and probe experiment, where the main effect of interest is the resonance shift, the pump wavelength is set at the resonance corresponding to the highest quality factor, in order to maximize the induced resonance shift.

So the pump wavelength is fixed at $\lambda_{0,\text{pump}}$, while the probe wavelength $\lambda_{\text{probe}}$ is fixed around its corresponding resonance $\lambda_{0,\text{probe}}$ with a small detuning. When two-photon absorption (TPA) and free-carrier absorption (FCA) occur, the pump pulse partially depletes and generates free electrons and holes. The CW probe monitors the resulting nonlinear temporal response of the ring.

The weak probe signal collected at the resonator output is detected by an avalanche photodiode (APD, Lab Buddy, bandwidth = 7 GHz) and recorded using a high-speed oscilloscope (Agilent Infinium 86100A, bandwidth = 50 GHz), after the residual pump pulses are removed by Filter 2 (JDS TB9 Optical Grating Filter). The measurements performed with the binary sequence were carried out using a different arbitrary waveform generator (AWG, Agilent 33220A) and an oscilloscope (Agilent DSO5034A) with a bandwidth of 300 MHz, suitable for bit rates below 60 Mbps.

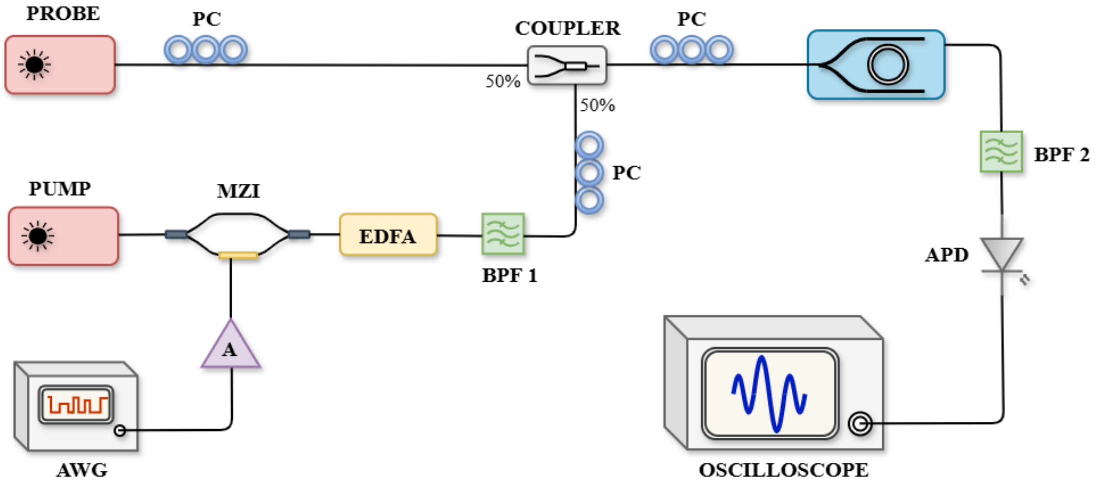

**Figure 4.1:** Experimental setup implemented in pump and probe measurements. The amplifier placed after the AWG is required to ensure the maximum modulation depth of the MZI. Polarization controllers (PC) are employed to optimize the optical power of both the pump and probe signals.

### 4.0.2 Pulse response measurements

By using short high-power pump pulses, it is possible to generate a large number of free carriers inside the ring while keeping the self-heating effect negligible. For such short pulses, the resulting temperature increase is estimated to be on the order of $m$K, allowing the pump–probe technique to isolate predominantly carrier-induced nonlinear effects. However, as will be shown later, when longer pump pulses are employed, the thermal contribution is no longer negligible and must be taken into account.

In the pulse response measurements, different pump pulse width were investigated, namely 100 ns, 1 ns, and 100 ps. Each measurement was performed by sending a single pulse with the desired width and a sufficiently long period between consecutive pulses, allowing the thermal effect to fully dissipate and all free carriers to recombine before the arrival of the next pulse. In this way, the temporal response to each pulse is not affected by the previous one.

In the model, the traps densities for silicon and polysilicon were set to fit the experimental measurements, as reported in Table 4.1.

**Table 4.1:** Traps densities for silicon and polysilicon implemented in the model.

| **Parameter** | **Material** | | **Unit** |
|---|---|---|---|
| | **Si** | **PolySi** | |
| Traps densities | $4.89 \times 10^{15}$ | $5.36 \times 10^{17}$ | $\mathrm{cm}^{-3}$ |

### 4.0.3 100 ns pulse width

For the 100 ns pulse measurements, a periodic pump waveform was applied, consisting of high-level optical pulses lasting 100 ns, followed by a low-level interval completing a total period of 1.6 $\mu$s. The estimated peak power was approximately 17 dBm. Figure 4.2 shows the pump signal trace measured with the oscilloscope, while Figure 4.3 reports the probe signal traces for different detuning values $\delta\lambda$.

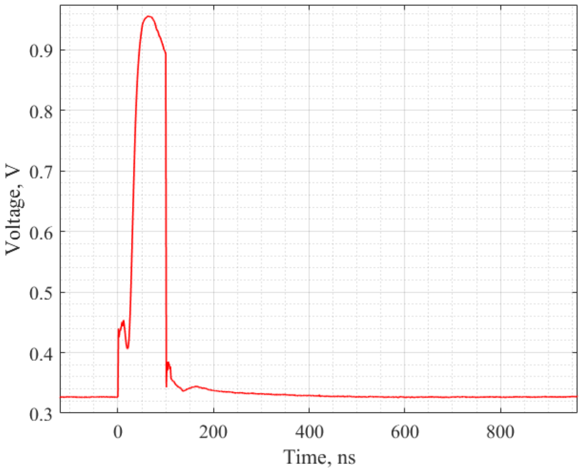

**Figure 4.2:** Measured pump optical pulse at the output of the microring resonator, with 100 ns duration.

For the probe trace a few detuning cases are analyzed in order to understand the behavior of non linear effects and temperature and how they interact with each other. To better understand the behavior of the pump and probe traces, it is necessary to analyze the individual contributions by means of the model. As shown in Figure 4.4, the model simulations accurately fit the measured probe traces obtained in the laboratory. Any small mismatches can be attributed to non-optimal biasing of the MZI. The model provides useful information for studying the behavior of the ring resonator. Let's first analyze the case of detuning $\delta\lambda = -0.6nm$ reported in Figure 4.4a.

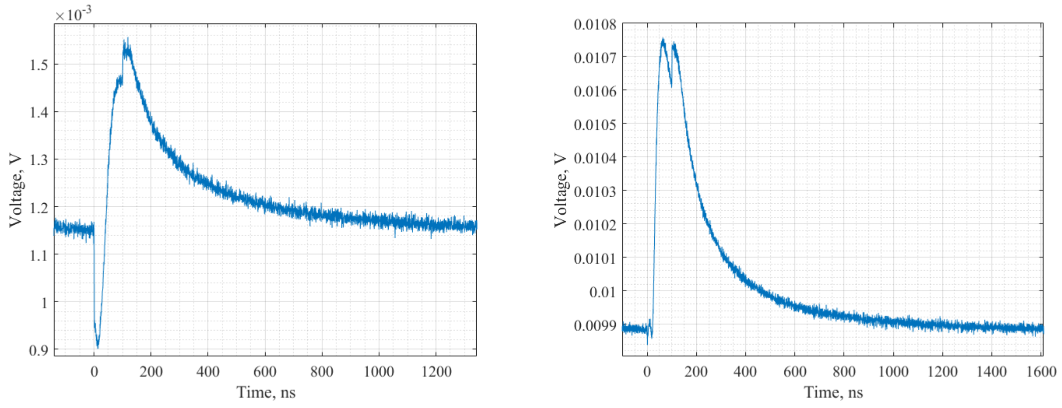

**(a)** $\delta\lambda = -0.6$ nm **(b)** $\delta\lambda = 0$ nm

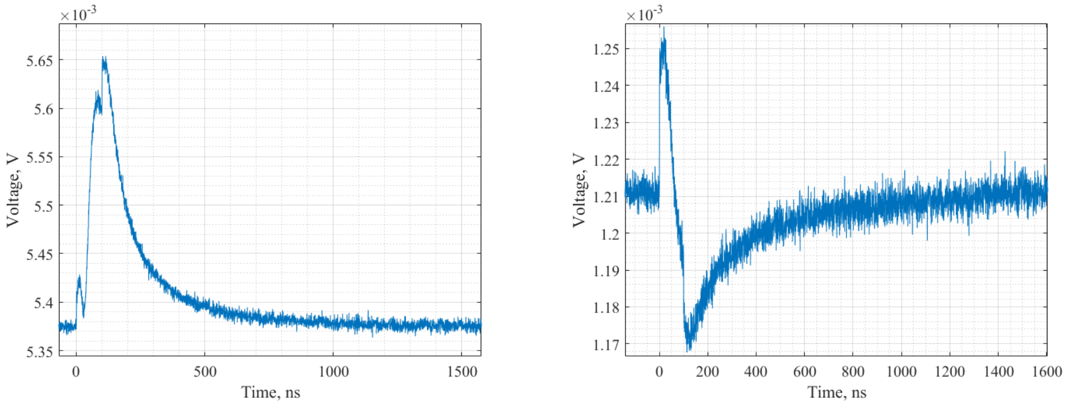

**(c)** $\delta\lambda = 0.1$ nm **(d)** $\delta\lambda = 0.6$ nm

**Figure 4.3:** Probe traces measured for different detuning values during 100 ns pump pulses.

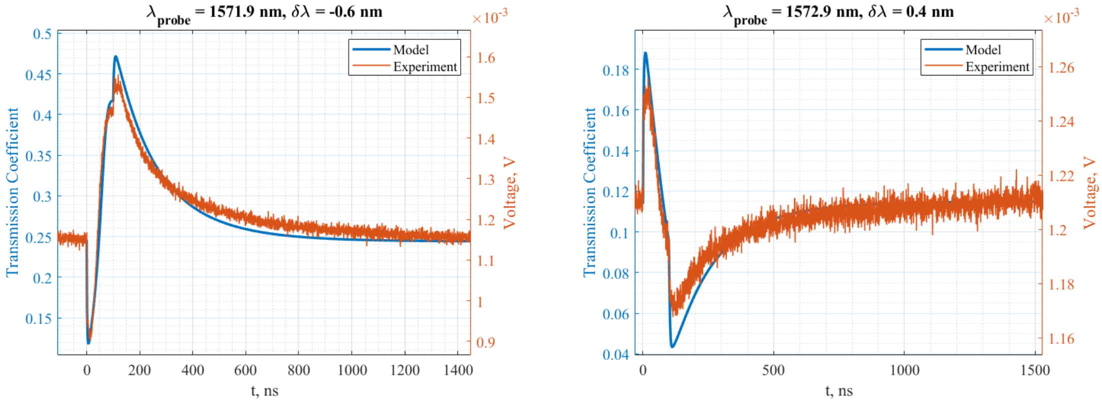

**(a)** $\delta\lambda = -0.6$ nm **(b)** $\delta\lambda = 0.4$ nm

**Figure 4.4:** Fitting of the model on the probe traces measured in laboratory for two values of detuning $\delta\lambda$.

In Figure 4.5 the temporal evolution of the circulating powers of both the pump and probe signals can be analyzed: at the beginning of the pulse, the resonance is at its cold position $\lambda_0$, which allows the circulating pump power to quickly reach its peak. Subsequently, as the circulating power increase, the concentration of free carriers increase rapidly as show in Figure 4.6 and the resonance shifts to the left due to the Free-Carrier-Dispersion effect, causing the pump signal to become detuned from the resonance, and consequently the circulating power decreases. When the resonance returns to its cold position because of the thermal effect, the circulating power increases again due to the realignment between the pump wavelength and the resonance. After the end of the pulse, the circulating pump power returns to zero. The probe circulating power, on the other hand, is never completely switched off and follows the evolution of the resonance shift over time.

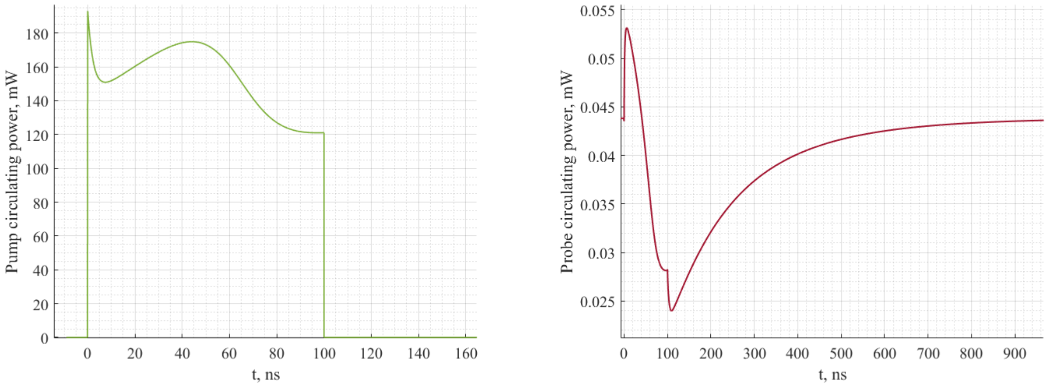

**(a)** Circulating pump power.

**(b)** Circulating probe power.

**Figure 4.5:** Temporal evolution of the circulating powers for the pump and probe signals during a 100 ns pump pulse.

Analyzing the carrier dynamics in Fig. 4.6, once the resonance has shifted to the left, the carrier density grows more slowly, due to the reduced circulating power in the ring. When the resonance returns to the cold resonance because of the thermal effect, the circulating power increases again, leading to a peak in carrier density. After this point, the temperature continues to rise, shifting the resonance further to the right. The circulating power then decreases, reducing both carrier generation and the FCD contribution.

By examining the contributions of the FCD and temperature to the resonance shift during the pulse duration, it can be observed that the thermal effect is very strong for long pulses, even for the same optical power, as will be shown later for shorter pulse durations. During the pulse, the ring experiences a temperature increase of approximately $14K$, as shown in Fig. 4.7a.

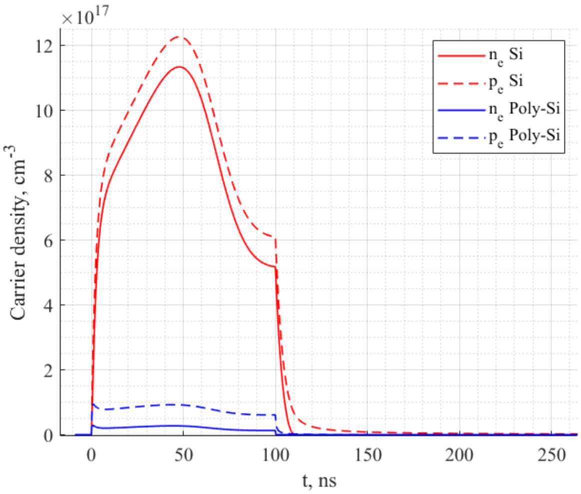

**Figure 4.6:** Carrier density dynamic during a 100 *ns* pulse.

Analyzing the resonance shift in Fig. 4.7b and the contributions of Free-Carrier Dispersion and thermal effects on the variation of $n_{\text{eff}}$ in Fig. 4.8, it can be seen that between 0 and 40 ns the FCD dominates, causing a left shift of the resonance, and consequently a decrease in the probe transmission. Gradually, the temperature increases and compensates for the FCD induced variation of $n_{\text{eff}}$, driving the resonance back to its initial position (cold resonance).

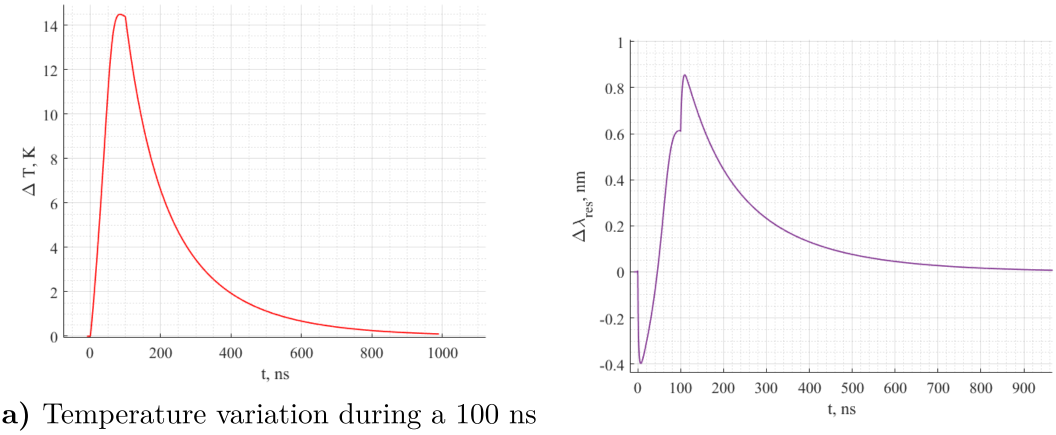

**(a)** Temperature variation during a 100 ns pulse.

**(b)** Resonance shift during a 100 ns pulse.

**Figure 4.7:** Temporal evolution of temperature and resonance shift during a 100 ns pump pulse.

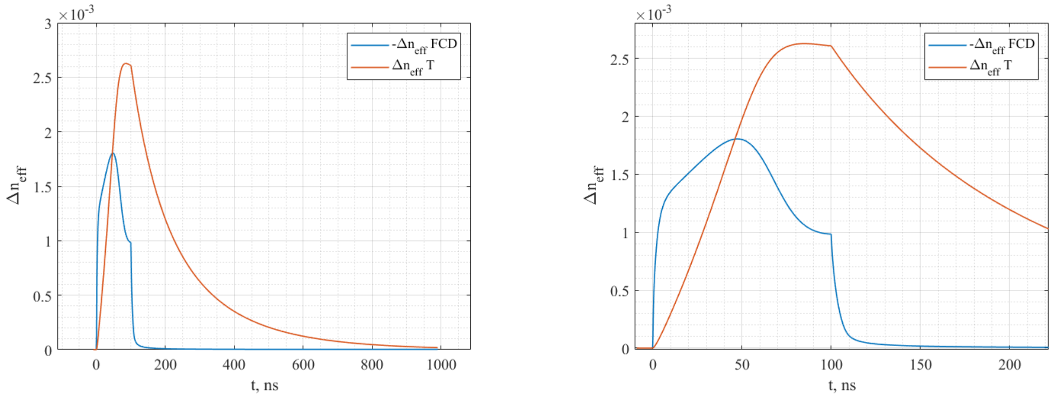

**(a)** **(b)**

**Figure 4.8:** Comparison between the effects of free-carrier dispersion (FCD) and temperature on the variation of the effective refractive index $n_{eff}$ during a 100 ns pump pulse. (a) Full time scale; (b) zoom on the pulse duration.

After the end of the pulse, carriers recombine much faster than the thermal dissipation time, resulting in a rapid rightward shift of the resonance at the falling edge of the pulse, leading to a fast increase in the probe transmission.

For the probe detuning case of $\delta\lambda = 0.4$ nm in figure 4.4b it can be observed that, at the beginning of the pulse, the probe transmission increases due to the resonance shift toward longer wavelengths caused by the FCD effect. Subsequently, the transmission decreases as the thermal effect induces a resonance shift in the opposite direction.

### 4.0.4 1 ns pulse width

For the 1 ns pulse measurement, pump pulses with a duration of 1 ns and a period of 100 ns were applied. As in the previous case, the following figures show the pump signal from the output of the ring and the probe traces for two different detuning values.

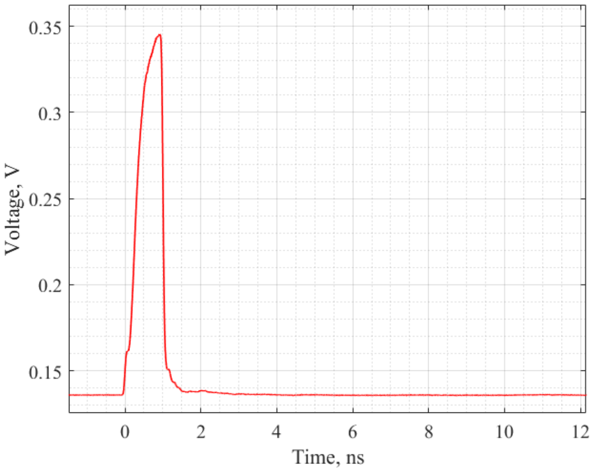

**Figure 4.9:** Measured pump optical pulse at the output of the microring resonator, with 1 ns duration.

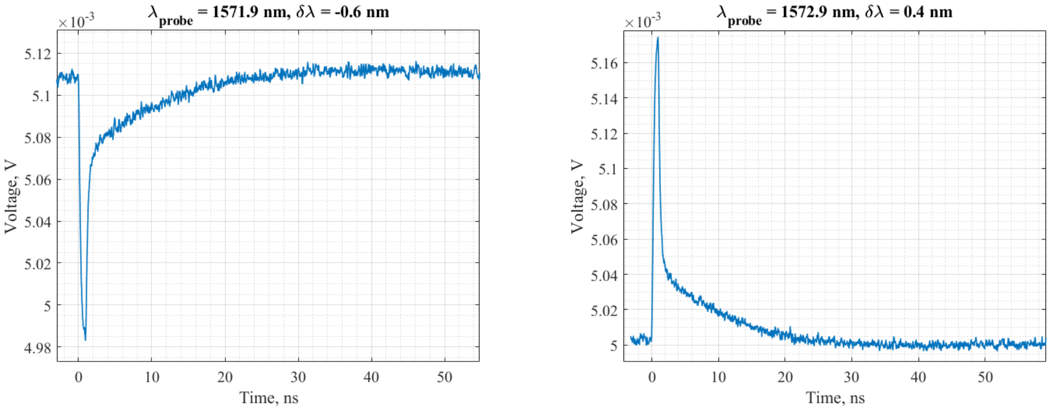

**(a)** $\delta\lambda = -0.6$ nm

**(b)** $\delta\lambda = 0.4$ nm

**Figure 4.10:** Probe traces measured for different detuning values during 1 ns pump pulses.

For the 1 ns case, only one detuning condition is analyzed. As shown in

Figure 4.11, the model fits reasonably well the experimental probe trace measured in the laboratory for a detuning of $\delta\lambda = -0.6$ nm.

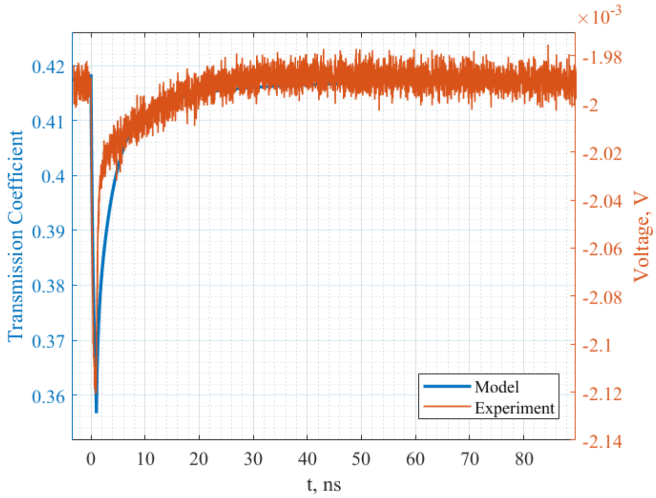

**Figure 4.11:** Fitting of the model on the probe trace measured in laboratory for $\delta\lambda = -0.6nm$.

The most relevant informations extracted from the model are shown in Figure 4.12. The temperature variation during the pulse is drastically reduced respect to the case of 100 $ns$ pulse width, reaching a peak value of only 0.09 $K$, making the thermal effect almost negligible. The resonance shift is also much smaller, with a maximum left shift of about $-0.2$ $nm$. Neglecting the thermal effect, the resonance shift back toward its initial position is only due to carrier recombination as we can see from the Figure 4.12d.

The smaller resonance shift can be attributed to a lower concentration of free carriers generated during the pulse, as shown in Figure 4.12c.

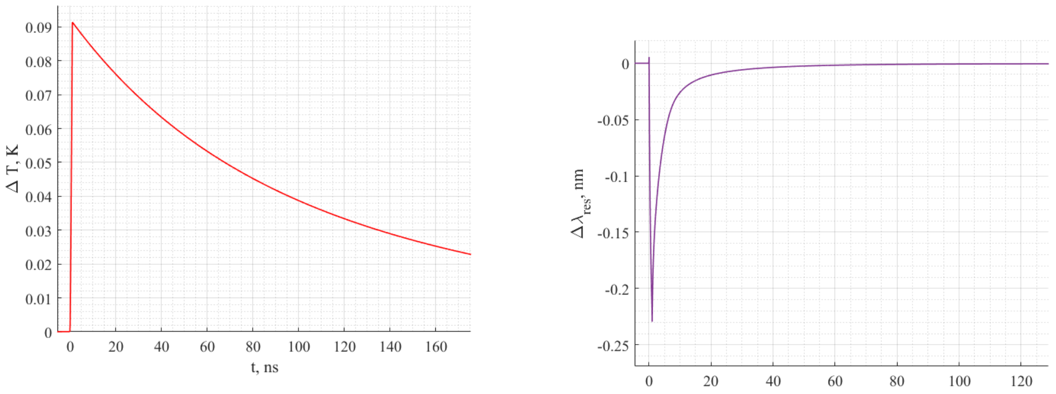

**(a)** Temperature variation during a 1 ns pulse.

**(b)** Resonance shift during a 1 ns pulse.

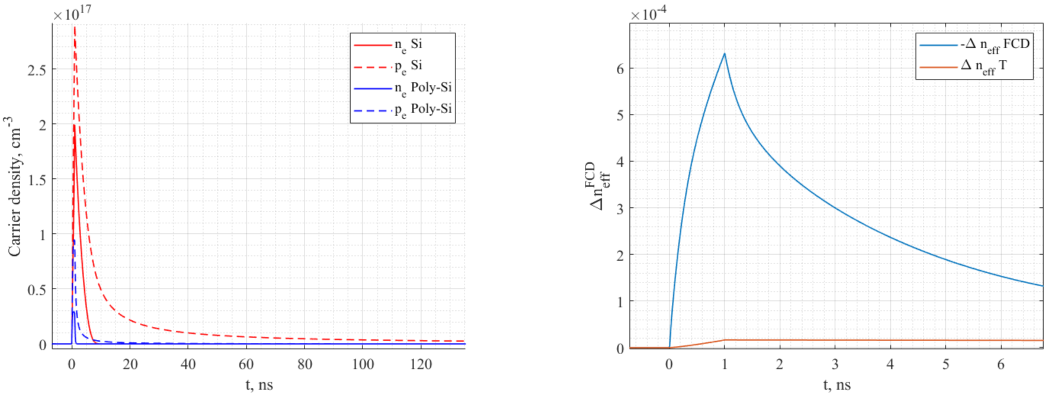

**(c)** Carrier density dynamics during a 1 ns pulse.

**(d)** Comparison between FCD-induced and thermal-induced $\Delta n_{eff}$ during a 1 ns pulse.

**Figure 4.12:** Temporal evolution of temperature, resonance shift, carrier density, and effective index variation during a 1 ns pump pulse.

### 4.0.5 100 ps pulse width

For the 100 ps pulse measurements, consecutive pump pulses with a duration of 100 ps and a period of 25 ns were applied.

In the following, the traces of the pump signal at the ring output and the probe signal for two different detuning values are reported.

Also in this case, the model accurately fits the measured probe trace as shown in Figure 4.14.

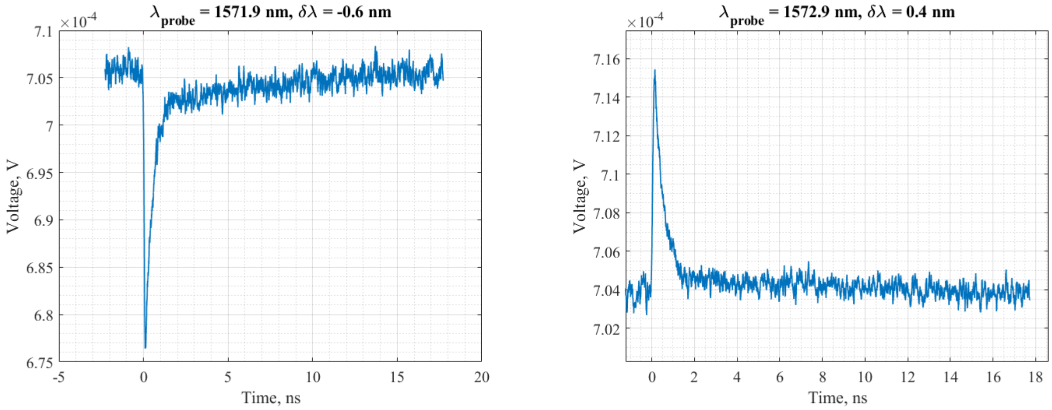

**(a)** $\delta\lambda = -0.6nm$ **(b)** $\delta\lambda = +0.4nm$

**Figure 4.13:** Probe traces measured for different detuning values during 100 ps pump pulse.

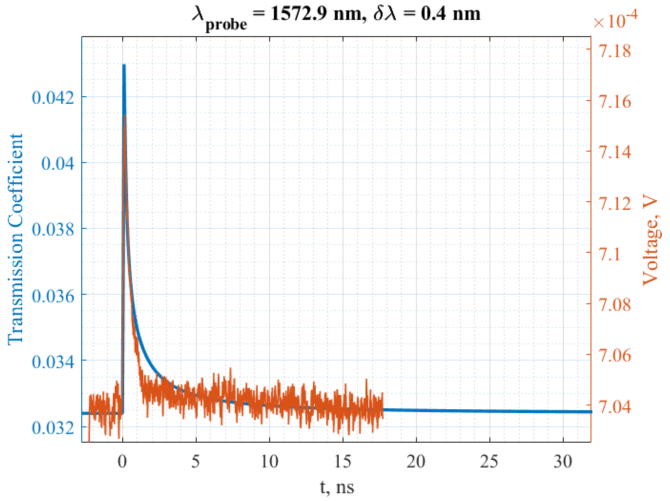

**Figure 4.14:** Fitting of the model on the probe trace measured in laboratory for $\delta\lambda = 0.4nm$.

Regarding the $100ps$ pump pulse, it can be observed that shortening the pulse duration reduces both the resonance shift and the peak temperature variation as shown in figure 4.15, as a consequence of the lower carrier concentration generated inside the ring. From previous works [5], and consistently with the $100ps$ pulse measurement, it is possible to extract the initial carrier lifetimes in silicon and polysilicon waveguides, as show in table 4.2.

**Table 4.2:** Experimental initial carrier lifetimes in Si-PolySi ring resonator, from [5].

| $\tau$ [ns] | **Silicon** | **Polysilicon** |
|---|---|---|
| $\tau_n$ | 6.4 | 0.17 |
| $\tau_p$ | 7.7 | 0.20 |

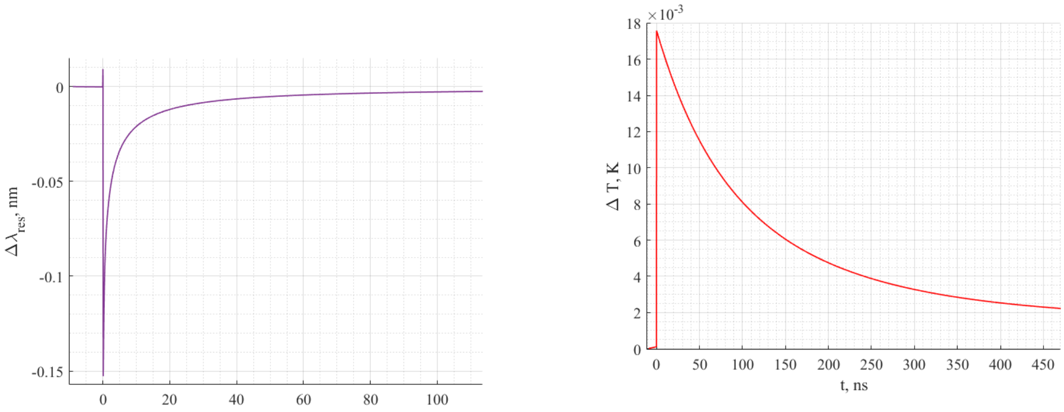

**(a)** Resonance shift during a 100 ps pulse.

**(b)** Temperature variation during a 100 ps pulse.

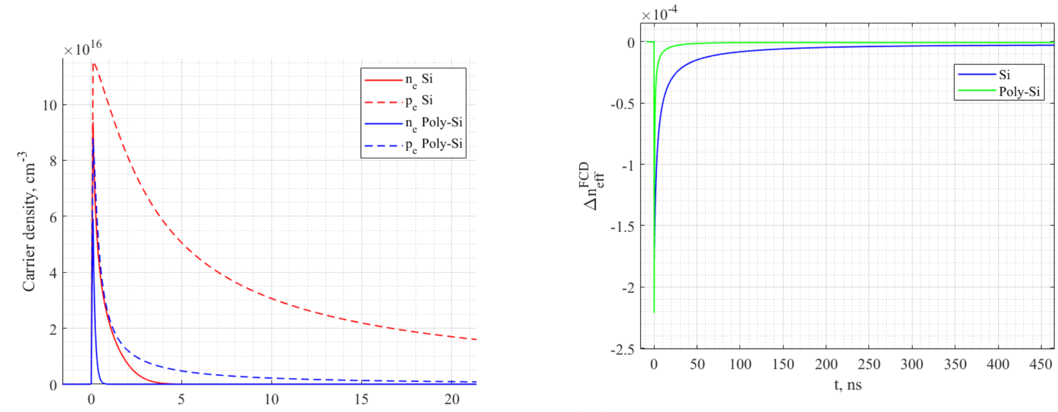

**(c)** Carrier dynamics during a 100 ps pulse.

**(d)** $\Delta n_{\text{eff}}$ induced by the PolySi and Si slab waveguide during a 100 ps pulse.

**Figure 4.15:** Temporal evolution of resonance shift, temperature variation, carrier density and effective index variation during a 100 ps pump pulse.

We observe that in polysilicon the free-carrier lifetime is strongly reduced due to the high density of trap states, which leads to faster carrier recombination. As a consequence, the effective refractive-index variation induced by the polysilicon region exhibits a much more rapid initial response compared to crystalline silicon, as illustrated by the fast initial transient in Fig. 4.15d.

## 4.1 XOR sequence

After analyzing the response to single pump pulses, the next step is to investigate the behavior of the probe trace under a bit sequence, with the goal of evaluating the suitability of the ring resonator for neuromorphic computing applications.

The measurements were performed by driving the AWG with a sequence of 5000 random bits, separated by 100 zeros in order to clearly identify the beginning and the end of the sequence on the oscilloscope. The estimated bus power for each measurement is approximately 10 dBm.

Measurements were carried out at different bitrates in order to better observe the dynamic behavior of the ring.

In figure 4.16 a portion of the experimentally measured trace at 10 Mbps with a probe detuning of $\delta\lambda_{\text{probe}} = 0.4$ nm is shown, together with the corresponding model simulation.

For the simulation, a peak power of 11 dBm was used instead of the 13 dBm measured experimentally. This value was obtained by evaluating the average optical power of the bit sequence and considering its 50:50 duty cycle. In the simulation, the probe detuning was set to 0.02 nm.

The discrepancy between the experimental and simulated detuning values is attributed to the different thermal dynamics occurring at the beginning of the bit sequence. In the experiment, the injected optical power during the initial portion of the sequence is temporarily higher as reported in figure 4.17, because of the EDFA gain dynamics. This transient power behavior induces an additional thermal red shift, causing the resonance to move further to the red compared to the simulation.

In addition to the initial shift, both experiment and simulation exhibit a thermal red shift along the bit sequence. At 10 Mbps, the bit duration is long enough for each logical '1' to generate a significant amount of heat, pushing the resonance toward longer wavelengths. Logical '0's provide partial thermal relaxation, and the temperature decreases only when sufficiently long zero intervals are present. On the other hand, an isolated '0' does not allow enough time for cooling, so the resonance remains thermally shifted. As shown in Fig. 4.18, the heat generated during each '1' is not fully dissipated before the next bit arrives, leading to a cumulative temperature rise and a gradual drift of the resonance. The ring returns to its cold position only after a sufficiently long sequence of logical '0's.

In Figure 4.19, the resonance shift and the carrier concentration over time are extracted from the simulation. From the resonance shift graph, the thermal red

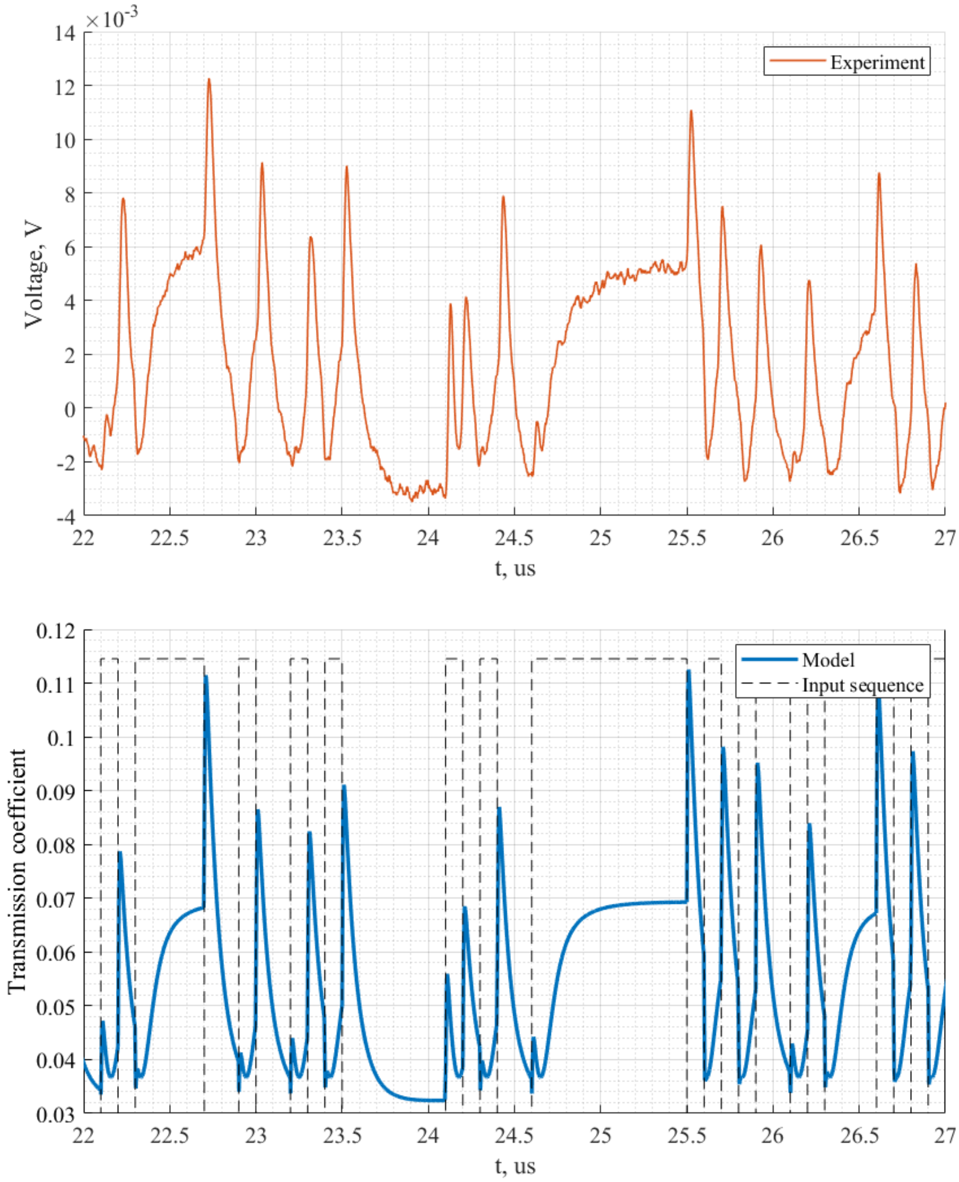

**Figure 4.16:** Experimental trace at 10 Mbps with $\delta\lambda_{\text{probe}} = 0.4$ nm (top) and corresponding model trace with $\delta\lambda_{\text{probe}} = 0.02$ nm (bottom).

shift caused by heat accumulation can be clearly seen. From the carrier dynamics, it can be observed that at a bitrate of 10 Mbps, the carrier lifetime in both silicon and polysilicon is sufficiently short for complete recombination before the coming of the successive bit. Therefore, since the FCD effect vanishes quickly, the discrepancy between the input sequence and the probe trace is solely due to the thermal effect.

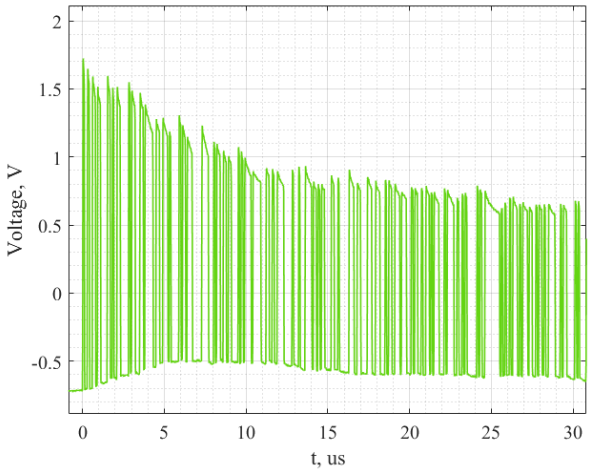

**Figure 4.17:** Initial transient of the pump bit sequence at the input of the ring. The transient exhibits a temporarily higher optical power, attributed to the EDFA gain dynamics.

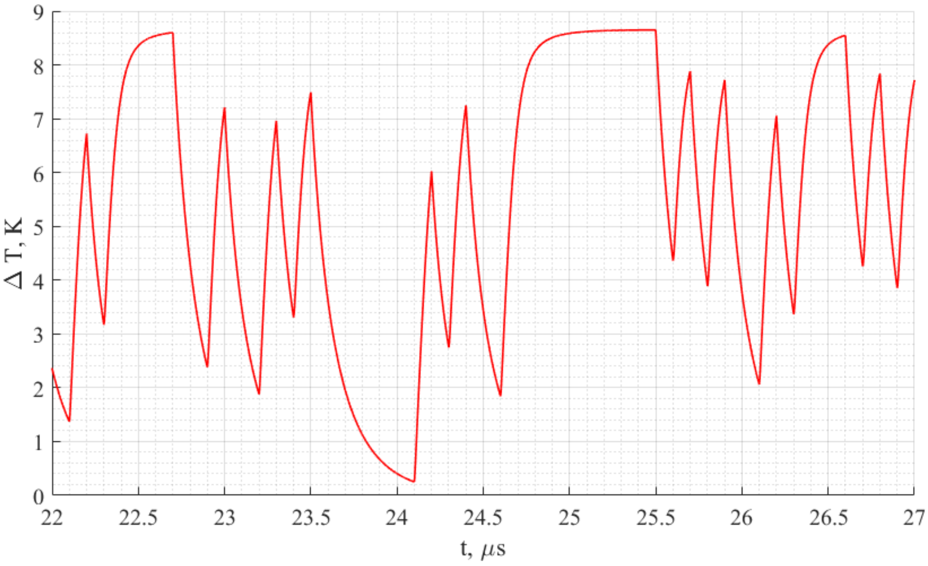

**Figure 4.18:** Thermal variation over time at 10 Mbps in the considered portion of the trace. It is evident that the accumulated heat is fully dissipated only after a sufficiently long sequence of zeros.

When the bitrate increases, the situation changes. Figure 4.20 shows the simulated probe trace at 500 Mbps, obtained with a peak power of 11 dBm and a

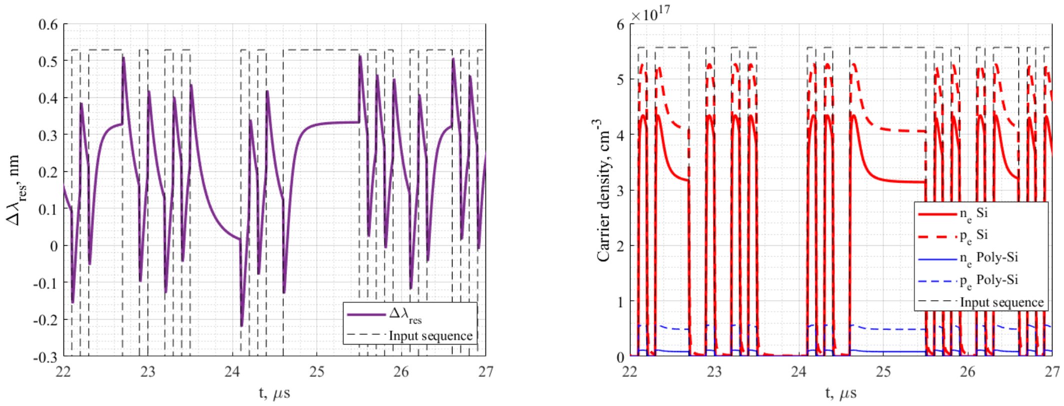

**(a)** **(b)**

**Figure 4.19:** (a) Resonance shift and (b) carrier dynamics over time for the 10 Mbps sequence.

probe detuning $\delta\lambda$ of 0.4 nm.

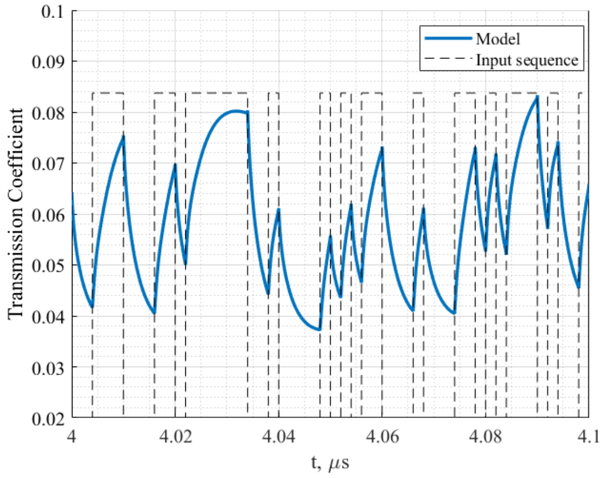

**Figure 4.20:** Simulated probe trace at 500 Mbps with $\delta\lambda = 0.4$nm.

The peak temperature, shown in figure 4.21a reached during each bit '1' decreases because the bit duration is shorter. Nevertheless, thermal dissipation becomes less effective: the zeros are now too short to significantly cool the ring. Therefore, a thermal shift is still present, but its variation over time becomes smoother. In other words, the temperature-induced variation of the effective index approaches a quasi-static value, instead of oscillating strongly as in the 10 Mbps case.

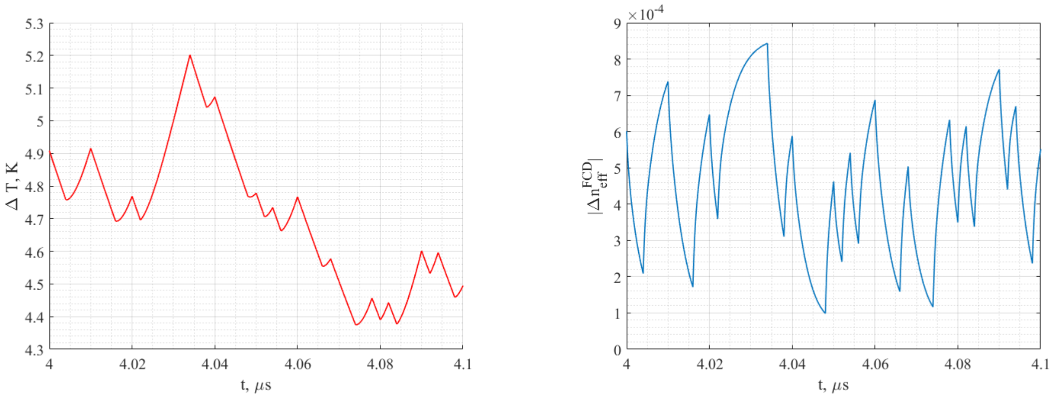

**(a)** Temperature variation over time at 500 Mbps.

**(b)** $|\Delta n_{eff}|$ induced by FCD over time at 500 Mbps.

**Figure 4.21:** Thermal and free-carrier–induced effective index variations at 500 Mbps.

This leads to an important consequence: at higher bitrates, the thermal contribution becomes almost constant, and the probe signal follows more closely the instantaneous resonance shift induced by FCD. In figure 4.21b, the temporal evolution of the effective index variation induced by FCD is shown in absolute value.

The figure 4.22 shows the simulation of the model for a probe trace at a bitrate of 2 Gbps. The most significant aspect in this case is the behavior of the contribution due to FCD shown in figure 4.23b.

At 2 Gbps, the probe trace mainly follows the variation of the effective index induced by FCD. However, since the carrier concentration generated in silicon is significantly higher than that in polysilicon, and because the carrier lifetime is much longer than the duration of a single bit at 2 Gbps, the carriers do not recombine completely before the arrival of the next bit.

As a result, a progressive accumulation of carriers in silicon occurs, leading to an increasing resonance shift caused by FCD, in addition to the nearly constant thermal shift.

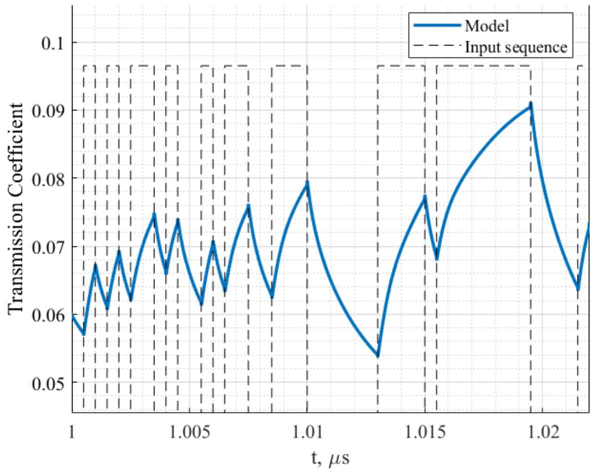

**Figure 4.22:** Simulated probe trace at 2 Gbps with $\delta\lambda = 0.4$nm.

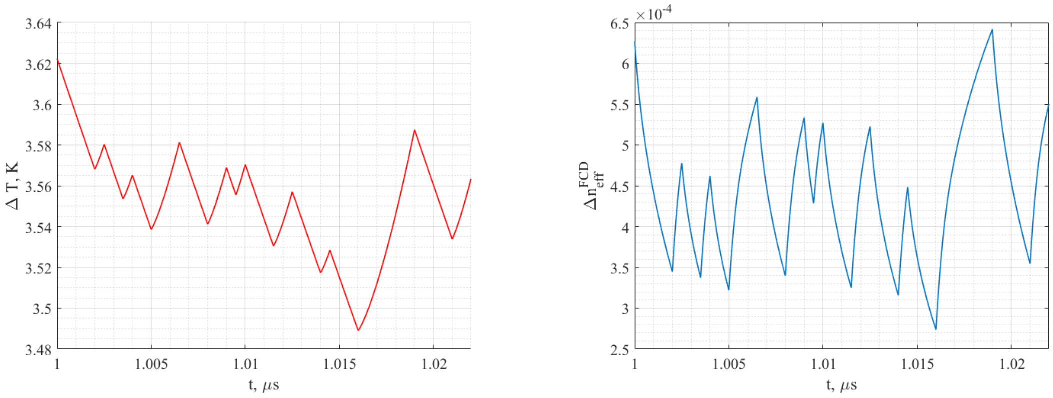

**(a)** Temperature variation over time at 2 Gbps.

**(b)** $|\Delta n_{eff}|$ induced by FCD over time at 2 Gbps.

**Figure 4.23:** Thermal and free-carrier–induced effective index variations at 2 Gbps.

By analyzing the probe trace at different bitrates, the following conclusions can be drawn regarding the thermal and carrier-induced dynamics of the Si-PolySi ring resonator:

- **Thermal effects at low bitrates:** At low bitrates, logical '1's generate high temperature peaks that significantly shift the resonance. The relatively long intervals between bits allow partial cooling, enabling the resonance to return close to its cold position. Hence, at low bitrates, the resonance shift cannot be attributed solely to FCD; thermal effects play a substantial role that highly

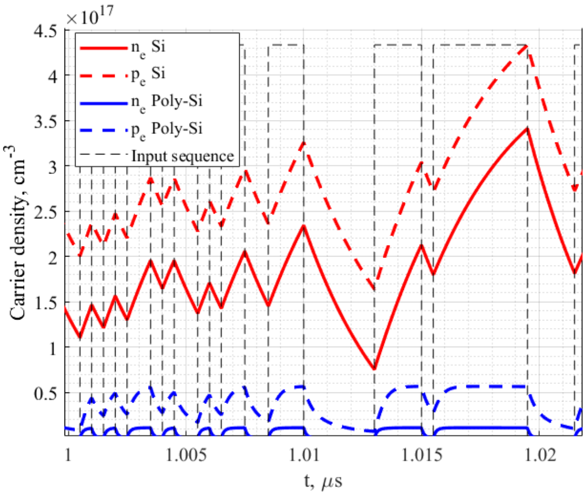

**Figure 4.24:** Carrier dynamics over time at 2 Gbps.

distorces the input bit sequence.

- **Thermal effects at intermediate bitrates:** As the bitrate increases, temperature peaks during logical '1's decrease, but the available cooling time is shorter. This results in a more persistent thermal red shift, which becomes relatively constant over time.
- **Carrier accumulation at high bitrates:** Above 500 Mbps, the bit duration is too short for complete carrier recombination in silicon. This leads to a steady FCD-induced resonance shift in addition to the thermal effect.
- **Impact on probe detuning:** The combined thermal and FCD shifts make the choice of probe detuning challenging, as the resonance position depends strongly on the bitrate. The detuning relative to the cold resonance loses practical significance.
- **Negligible polysilicon contribution at high bitrates:** At very high bitrates, carriers in polysilicon have a minor impact. Despite shorter carrier lifetimes in polysilicon, the higher carrier concentration in silicon dominates the resonance dynamics, rendering the polysilicon response negligible in the probe trace.
- **Measurability limitations:** As bitrate increases, the resonance shift follows the carrier concentration more closely, but its magnitude decreases. This reduces the measurability of the probe signal in the laboratory, particularly when using an avalanche photodetector.

# Chapter 5

# Neuromorphic Computing Application

## 5.1 1-Bit Delayed XOR

The 1-bit delayed XOR task consists of predicting the XOR of each bit in a binary sequence with its immediately preceding bit. Since the microring resonator operates as a continuous-time optical reservoir and only the readout layer is trained, a dedicated pre-processing and post-processing pipeline, developed in [3], is necessary. The following sections describe how the input sequence is encoded, how the reservoir states are extracted and organized, and how the linear readout is trained and evaluated.

### 5.1.1 Pre-processing

**Bit-stream generation and target construction**

A random binary sequence of 5000 bits is generated to form the input stream. For each bit, the XOR operation with the preceding bit is computed, yielding the target sequence. To enable supervised learning, the XOR outputs are converted to a one-hot representation:

$$\mathrm{XOR} = 0 \rightarrow [1\ 0]^T, \qquad \mathrm{XOR} = 1 \rightarrow [0\ 1]^T,$$

resulting in a $2 \times N$ label matrix for the entire sequence.

**Input encoding and virtual node expansion**

Each bit is converted into a continuous-time optical waveform by the microring modulator. Since the reservoir operates in continuous time, the optical waveform must be sampled to obtain discrete-time states. Each bit is uniformly sampled at $N_v$ time points, generating $N_v$ virtual nodes as shown in figure 5.1.

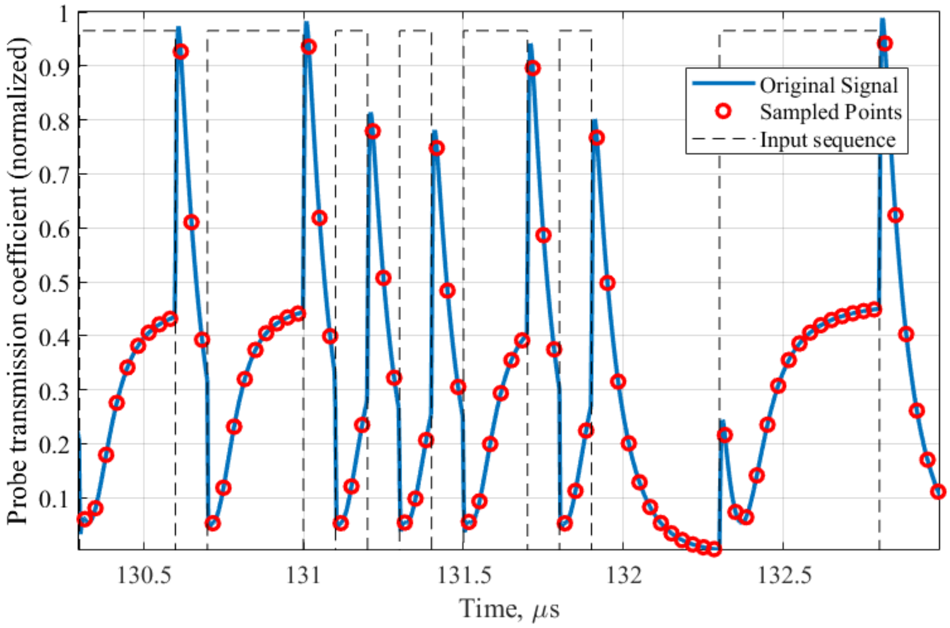

**Figure 5.1:** Example of sampling each bit of a probe out trace at 10 Mbps with 3 Nv.

The samples for each bit are stacked as a column vector to form the initial reservoir state matrix:

$$X \in \mathbb{R}^{N_v \times N_{\text{bits}}}.$$

Here, each column represents the reservoir response associated with one input bit. So, in the experiment $X$ has dimensions $3 \times 4998$ (for 3 virtual nodes per bit). The first two bits are discarded since they cannot be paired with a previous bit).

### State reordering for temporal dependency

The 1-bit delayed XOR task requires the system to retain information about the previous bit. To encode this temporal dependency, the state matrix $X$ is reorganized so that each training sample contains the virtual node responses of both the current bit and the previous bit.

Specifically, for bit index $i$, the samples corresponding to bit $i-1$ are concatenated on top of those of bit $i$, producing the final matrix:

$$X_{\text{final}} \in \mathbb{R}^{2N_v \times N_{\text{bits}}}.$$

The top $N_v$ rows contain the previous bit's states, and the bottom $N_v$ rows the current bit's states.

In our case, the matrix $X$ is first reshaped to $6 \times 2499$ by concatenating consecutive bits, and then further reorganized to $6 \times 4997$, ensuring that each bit appears in the correct temporal context: once as the previous bit and once as the current bit.

This final organization ensures that the readout layer can exploit the fading-memory effect of the reservoir, which is essential for the delayed-XOR computation.

### 5.1.2 Post-processing

#### Dataset splitting

The reorganized state matrix $X_{\text{final}}$ and the one-hot label matrix are divided into training and test sets to allow for proper evaluation on unseen sequences. The split is performed with a 70% training set and a 30% test set.

#### Linear readout training

Only the readout layer is trained using ridge regression:

$$W_{\text{out}} = \frac{Y_{\text{train}} X_{\text{train}}^T}{X_{\text{train}} X_{\text{train}}^T + \lambda I},$$

where $\lambda$ is the regularization parameter. This matrix $W$ maps the $2N_v$ virtual node states to the two output classes.

#### Classification and decoding

For each test sample, the trained readout produces a two dimensional output vector:

$$\text{output} = W_{\text{out}} X_{\text{test}}.$$

The predicted class is determined using a winner-take-all rule:

$$\hat{y}(i) = \arg\max_j \text{output}(j, i),$$

yielding the predicted XOR bit sequence.

#### Accuracy evaluation

The predicted sequence is compared with the ground truth to compute classification accuracy, bit-error rate, and confusion matrices. These metrics quantify the reservoir's ability to extract and generalize the temporal XOR relationship from the continuous-time dynamics.

## 5.2 Classification accuracy results

In this section, we analyze the classification results produced by the neural network for the 1-bit XOR predictor. Multiple traces of the same 5000 bit sequence were examined, varying both detuning of the probe signal and average pump power. Using the model, as we have seen, it is possible to replicate the probe output trace from the ring with reasonable similarity. This will be useful for estimating the upper bound of accuracy that the network can achieve.

Figure 5.2a shows the accuracies achieved by the neural network in solving the previously described task with $N_v$ equal to 3, both for the experimental traces and for the traces simulated by the model. For each trace, different detunings $\delta\lambda_{probe}$ were considered, and the best result was taken. The experimentally measured average pump power is 10 dBm.

As observed, the experimental trace at low bitrates does not achieve sufficiently high accuracy to consider the experiment successful. In contrast, the model yields significantly higher accuracies, up to 96%. This demonstrates how laboratory measurements are affected by non-idealities that strongly impact accuracy results, such as coupling losses, the nonlinear gain dynamics of the EDFA, incorrect polarization optimization and improper biasing of the MZI.

The trace at 50 Mbps, for which both experimental and theoretical results reach approximately 92% accuracy, indicates that the experiment is nonetheless feasible In figure 5.3 the extracted confusion matrix is reported.

Figure 5.2b illustrates how the choice of the number of virtual nodes plays a crucial role in determining the accuracy of the results. In general, selecting the number of nodes represents a trade-off between the required complexity of information processing, which typically increases with $N_v$, and the operational speed [10].

Increasing the number of virtual nodes from 3 to 6 leads to slightly higher accuracies.

Using the model, it is possible to obtain the probe output traces at high bitrates, since, as previously explained, experimental measurements at these bitrates were not feasible due to APD noise and the very weak signal resulting from very small resonance shifts. In figure 5.4 it is observed that the shorter carrier lifetime in polysilicon does not improve accuracy at high bitrates, as the performance drops above the GHz range. A slight improvement is seen at intermediate bitrates (100–500 Mbps), where, as discussed in section 4.1, the thermal effect is more stable. The different simulated traces where obtained with $N_v = 3$, the same detuning $\delta\lambda = 0.02nm$ and $P_{avg} = 10dBm$.

The following analysis examines how different average pump powers affect the accuracy. Two figures are reported in Fig. 5.5, showing both the experimental and theoretical accuracies obtained from the probe out traces at average pump

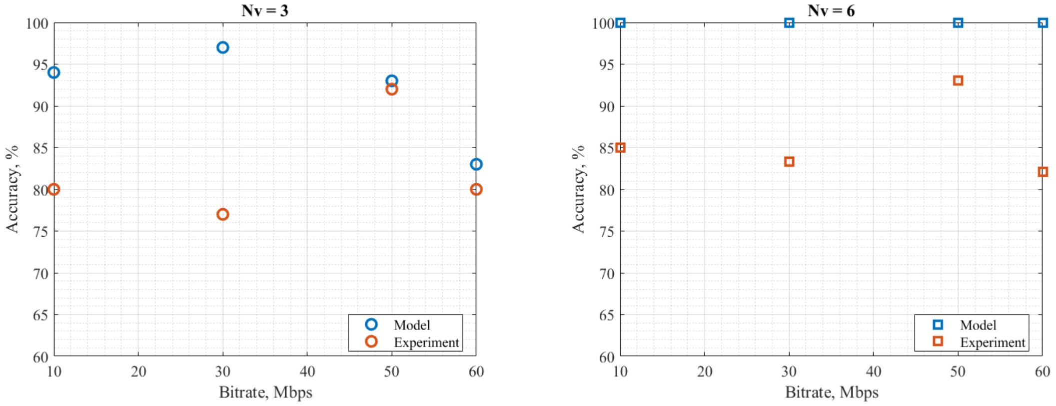

**(a)** Accuracy with 3 virtual nodes. **(b)** Accuracy with 6 virtual nodes.

**Figure 5.2:** Simulated and experimental results for $P_{avg} = 10dBm$. Increasing from 3 to 6 virtual nodes slightly improves the results.

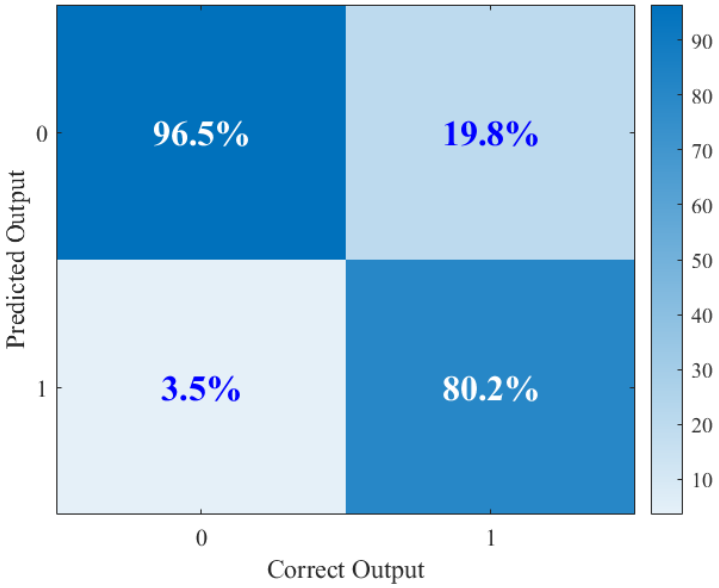

**Figure 5.3:** Confusion matrix obtained from the sampled measured probe signal with $P_{avg} = 10dBm$, $\delta\lambda = -0.1nm$ at $50Mbps$. The classification accuracy is 92%.

powers of 10 dBm and 6 dBm. The detuning was kept fixed at +0.1 nm in the experimental setup, which corresponds to −0.28 nm in the model because of the additional thermal shift already mentioned in 4.1. From the model results, it can be observed that reducing the average pump power and therefore the resonance

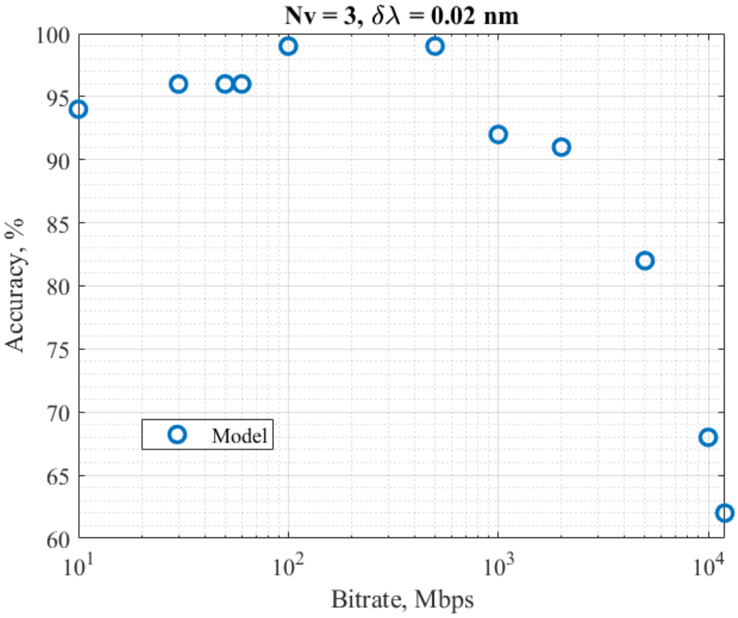

**Figure 5.4:** Accuracy obtained from the model at various bitrate.

shift and the thermal effects, allows achieving 100% accuracy even when using only $N_v = 3$. On the other hand, in the experimental measurements, lowering the pump power leads to a noisier probe out trace, and consequently the accuracy degrades rather than improving.

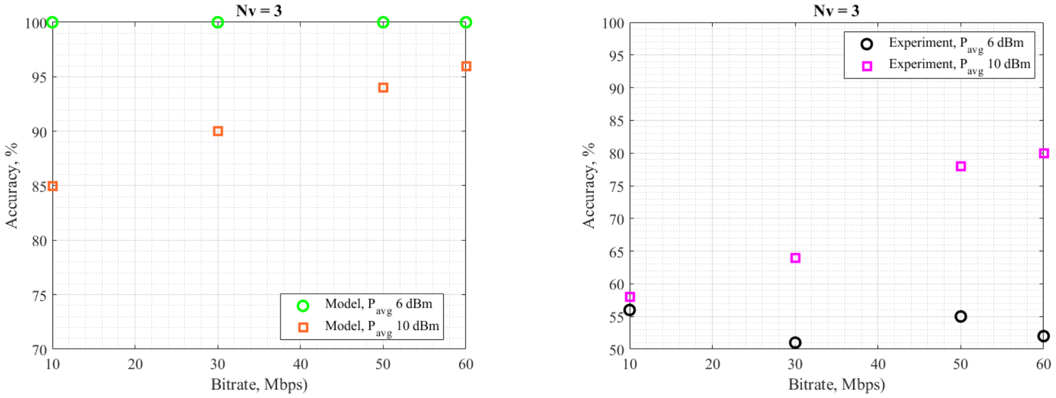

**(a)** Model accuracy at different average pump powers.

**(b)** Experimental accuracy at different average pump powers.

**Figure 5.5:** Classification accuracy comparison between model and experimental accuracies for two average pump powers. Detuning is +0.1 nm experimentally, corresponding to -0.28 nm in the model.

Finally, a comparison is made with the results obtained using the pure silicon ring presented in [3]. In Fig. 5.6, the low-bitrate classification accuracy is reported for the input pump trace, the Si probe-out trace, and the Si–PolySi probe-out trace. For the Si–PolySi device, results are shown for both 6 dBm and 10 dBm average pump power, while keeping a fixed detuning of $\delta\lambda = 0.1\,\text{nm}$ for all the analyzed bitrates. The results clearly indicate that, even when increasing the pump power from 6 dBm to 10 dBm, the experiment with the silicon–polysilicon ring does not succeed. The classification accuracy obtained from the probe out signal remains lower than that of the input pump trace, demonstrating that the ring does not provide any computational benefit under these operating conditions.

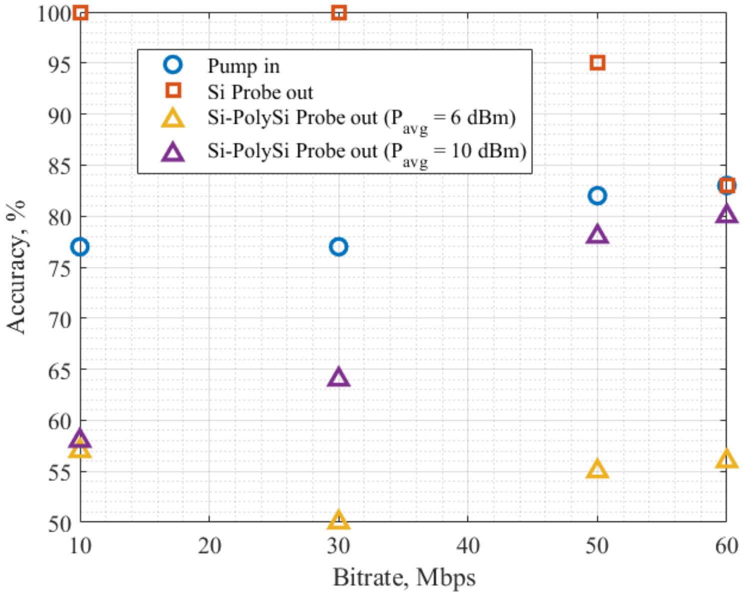

**Figure 5.6:** Classification accuracy comparison between Si MRR and Si-PolySi MRR.

# Chapter 6

# Conclusions

In this work, the previously developed pump and probe setup and theoretical model were extended to the case of a different microring resonator. The experimental procedure was adapted to characterize and analyse the dynamics of a hybrid Si-PolySi microring resonator. In particular, the model was extended to reproduce the response of the ring under bit-sequence excitation, enabling the extraction of detailed information on the free-carriers and thermal dynamics, showing how these effects shape the device response across different bitrates.

At low bitrates, logical '1' bits generate significant temperature peaks, producing resonance shifts that are not negligible; despite partial cooling between bits, thermal dynamics still introduce substantial distortions in the sequence at the output of the MRR that depends strongly on the choice of the detuning of the probe signal. As the bitrate increases, these temperature excursions diminish, yet the reduced cooling time leads to a persistent thermal red shift that gradually approaches a quasi-steady value.

At higher bitrates (above approximately 500 Mbps), the bit period becomes too short for complete carrier recombination in silicon, resulting in carrier accumulation and a sustained FCD induced shift superimposed on the thermal contribution. This combined effect complicates the choice of probe detuning, as the resonance position becomes strongly dependent on the bitrate, making detuning relative to the cold resonance largely impractical. Moreover, although carriers in polysilicon recombine more rapidly, their contribution becomes negligible at very high bitrates, where the higher silicon carrier density dominates the refractive-index dynamics.

Finally, as the bitrate increases further, the resonance shift follows the carrier density more closely while decreasing in magnitude, reducing the visibility of the probe modulation and ultimately limiting the measurable signal in laboratory conditions, particularly when using avalanche photodetectors.

The results obtained for the 1-bit delayed XOR task further illustrate the limitations imposed by the strong dependence of the resonance position on the bitrate, which complicates the choice of probe detuning. As a consequence, the experimental traces do not consistently yield high classification accuracies when using a fixed detuning. At 50 Mbps, for instance, an average pump power of 10 dBm leads to a classification accuracy of approximately 92%. This confirms that, despite the strong thermal distortion affecting the waveform at low bitrates, the experiment remains feasible. Nevertheless, such performance does not reach the 100% accuracy observed with pure silicon microrings. The presence of polysilicon and its faster carrier dynamics does not provide any improvement; in the GHz range, the accuracy obtained from training the simulated bit sequences decreases from 93% at 1 GHz, to 82% at 5 GHz, and down to 68% at 10 GHz. At these high bitrates, the combined difficulties in selecting an optimal detuning, together with noise and other non-idealities (e.g., non-optimal setup conditions), make experimental measurements effectively impractical.

The traces obtained from model, by contrast, delivers higher accuracies, particularly at intermediate bitrates (100-500 Mbps), where the thermal effect becomes more stable than at very low bitrates. Achieving 100% accuracy requires increasing the number of virtual nodes: Raising $N_v$ from 3 to 6 is sufficient to achieve perfect accuracy in the simulations, with a slight improvement also observed in the experimental trace.

Additional simulations also show how different pump powers influence accuracy: reducing the pump power and thus decreasing both the resonance shift induced by FCD and the thermal effects enables 100% accuracy even with $N_v = 3$. Experimentally, however, lowering the pump power leads to a noisier probe trace, causing the accuracy to degrade rather than improve.

As future work, one potential direction is to optimize the design of the Si-PolySi microring in order to reduce its thermal impedance and consequently mitigate the dominant thermal effects observed in the current device. A possible approach is to decrease the distance between the slab waveguide and the substrate, which would enhance heat dissipation; however, this modification inevitably increases radiation losses, which must be carefully considered during the design process.

Another avenue for future research is to investigate the performance of this microring in the context of the IRIS species recognition task. In this scenario, it will be necessary to assess whether the dynamic response of the ring, including the thermo-optic and carrier-induced effects, is compatible with the computational requirements of the application, and whether structural optimizations could further improve overall efficiency and accuracy.

# Bibliography

[1] Herbert Jaeger. *The Echo State Approach to Analysing and Training Recurrent Neural Networks.* Tech. rep. GMD Report 148. With an erratum note. Bonn, Germany: German National Research Center for Information Technology (GMD), 2001 (cit. on p. 1).

[2] M. Borghi, S. Biasi, and L. Pavesi. «Reservoir computing based on a silicon microring and time multiplexing for binary and analog operations». In: *Scientific Reports* 11 (2021) (cit. on pp. 2, 43).

[3] Salvatore Salpietro. «Study of Microring Nonlinearities in Silicon Photonics for Neuromorphic Computing». MA thesis. Torino: Politecnico di Torino, 2024 (cit. on pp. 2, 5–7, 38, 43, 63, 69).

[4] S. Salpietro, M. Novarese, and et al. «Non-linear Effects in Silicon Photonics Microring for Reservoir Computing: Modeling and Experiments». In: *European Conference on Integrated Optics (ECIO).* European Conference on Integrated Optics ECIO 2025. Cardiff, Wales, 2025 (cit. on p. 2).

[5] Marco Novarese. «Modelling and characterisation of microrings for semicondunctor lasers integrated in the Silicon Photonics platform». PhD thesis. Torino: Politecnico di Torino, 2023 (cit. on pp. 2, 22, 54, 55).

[6] Wim Bogaerts et al. «Silicon Microring Resonators». In: *Laser Photonics Reviews* (2012), p. 2 (cit. on p. 11).

[7] Milos Nedeljkovic, Richard Soref, and Goran Z. Mashanovich. «Free-carrier electrorefraction and electroabsorption modulation predictions for silicon over the 1–14-m infrared wavelength range». In: *IEEE Photonics Journal, 3(6)* (2011), pp. 1171–1180 (cit. on p. 23).

[8] M. Webster, C. Appel, P. Gothoskar, S. Sunder, B. Dama, and K. Shastri. «Silicon photonic modulator based on a mos-capacitor and a cmos driver». In: *IEEE Compound Semiconductor Integrated Circuit Symposium (CSICS)* (2014), pp. 1–4 (cit. on p. 30).

[9] M. Novarese and et al. «Dynamics of Free Carrier Absorption and Refractive Index Dispersion in Si and Si/polySi Microrings». In: *IEEE Photonics Technology Letters* 35 (2023), p. 4 (cit. on p. 43).

[10] K. Takano et al. «Compact reservoir computing with a photonic integrated circuit». In: *Opt. Express* 26 (2018), pp. 29424–29439 (cit. on p. 66).